

Lyman-alpha haloes in the aftermath of reionisation

Daniil Smirnov^{1*}, Lutz Wisotzki¹, Tanya Urrutia¹, John Pharo¹, Ramona Augustin¹, Yucheng Guo², Daria Kozlova¹, Haruka Kusakabe³, Jorryt Matthee⁴, Ismael Pessa¹, and Joop Schaye⁵

¹ Leibniz-Institut für Astrophysik Potsdam (AIP), An der Sternwarte 16, 14482 Potsdam, Germany

² School of Earth & Space Exploration, Arizona State University, 781 Terrace Mall, Tempe, AZ 85287, USA

³ Department of General Systems Studies, Graduate School of Arts and Sciences, The University of Tokyo, 3-8-1 Komaba, Meguro-ku, Tokyo, 153-8902, Japan

⁴ Institute of Science and Technology Austria (ISTA), Am Campus 1, 3400 Klosterneuburg, Austria

⁵ Leiden Observatory, Leiden University, PO Box 9513, 2300 RA Leiden, the Netherlands

Received XXX; accepted YYY

ABSTRACT

We present a comparative study of Ly α haloes (LAHs) around low-luminosity ($L_{\text{Ly}\alpha} \lesssim 10^{42}$ erg s⁻¹) Ly α -emitting galaxies (LAEs) at very high redshifts $z \geq 6$ and a reference sample at $z \sim 3$ covering a similar Ly α luminosity and host galaxy stellar mass range. Using data from the Multi-Unit Spectroscopic Explorer (MUSE) at the ESO VLT, we extracted the samples such that at the different redshifts we obtain the same *intrinsic* surface brightness sensitivity, accounting for cosmological dimming. We detect extended Ly α emission around 6 out of 18 high- z LAEs in the MUSE eXtremely Deep Field (MXDF), more than doubling the number of known such objects at $z \geq 6$. We obtain an only slightly higher individual LAH detection fraction of 40% among the lower redshift comparison sample. Yet the typical exponential scale lengths at $z \geq 6$ are three times smaller than those at $z \sim 3$. Stacking the LAEs with undetected haloes gives again drastically different results for the two samples, with a highly significant halo detection at $z \sim 3$ but no trace of extended Ly α emission at $z \geq 6$. We also find the Ly α spectral line widths of the high- z sample to be ~ 2.5 smaller in comparison to the lower redshift objects. We discuss the potential mechanisms driving such strong changes. In a reionisation-driven scenario the higher neutral fraction in the intergalactic and circumgalactic media might lead to substantial scattering losses of escaping Ly α radiation, leaving detectable only emission from the vicinity of the star-forming regions. In an alternative scenario the LAH properties might be linked more closely to the evolution of their host galaxies than previously thought.

Key words. galaxies: evolution – galaxies: high-redshift – galaxies: CGM – cosmology: reionisation

1. Introduction

The Ly α emission line is one of the principal tracers of star-forming galaxies at high redshifts (Partridge & Peebles 1967). It is now well established that this emission is not confined to the sites of actual star formation, but often extends far beyond the stellar components of galaxies. Typically more than half, and sometimes even more than 90% of the total Ly α luminosity of a galaxy emerges from this circumgalactic region (Wisotzki et al. 2016, Leclercq et al. 2017 hereafter cited as LW16 and FL17, respectively). The physical mechanisms to produce these Ly α haloes (LAHs) can be diverse, but the dominant process is probably recombination radiation followed by resonant scattering at H I clouds in the circumgalactic medium (CGM) (e.g., Verhamme et al. 2006, Kusakabe et al. 2019, Mitchell et al. 2021, Byrohl et al. 2021). LAHs are therefore valuable tracers of the cool and partly neutral CGM at high redshifts.

Recent years have seen a tremendous push of the observational frontier towards earlier cosmic epochs and into the epoch of reionisation. The visibility of Ly α in galaxies at very high redshifts is now one of the key probes of the rapidly evolving H I content of the Universe (e.g., Ouchi et al. 2020, Napolitano et al. 2024, Runnholm et al. 2025). While the internal production of Ly α radiation depends mainly on the star formation rate, its escape and propagation along the line of sight can be greatly re-

duced through scattering. Predicting the shape and the spatial extent of Ly α emission during reionisation is challenging (e.g., Ahn & Shapiro 2021, Melia 2024, Kageura et al. 2025 and references therein), but qualitatively, an immediate consequence of a more neutral medium surrounding a Ly α -bright galaxy would be to disperse its line emission, both spatially and spectrally. A large neutral fraction in the CGM or in the adjacent intergalactic medium (IGM) would therefore cause the solid angle of Ly α emission to spread out and render the emission essentially invisible (unless the system resides in a substantial ionized bubble; e.g., Witstok et al. 2025). On the other hand, an only moderately increased abundance of neutral gas in the outskirts of a galaxy at the end of reionisation might lead to just a more extended LAH, still observable albeit with lower surface brightness.

Measurements of the prominence and properties of Ly α haloes could thus provide additional constraints on the reionisation process and topology, especially its late stages at $z \sim 6-7$. Observational data on LAHs at these redshifts are however scarce, with currently only very few known haloes at $z \geq 6$ (Ouchi et al. 2009, FL17, Shibuya et al. 2018, Matthee et al. 2020b, Zhang et al. 2020). Some of these are extremely luminous ($L_{\text{Ly}\alpha} > 10^{43}$ erg s⁻¹) and fall into the category of Ly α “blobs”, with counterparts that show complex clumpy merger UV morphology and tentative AGN signatures (Marconcini et al. 2025, Kiyota et al. 2025), making them more akin to Ly α nebulae around QSOs (e.g., Borisova et al. 2016, Farina et al. 2017, Arrigoni Battaia et al. 2019). Statistical stud-

* Corresponding author: dsmirnov@aip.de

ies of haloes around star-forming galaxies at this redshift are also limited. Momose et al. (2014) found an extended Ly α halo in a stack of 119 narrowband images of Lyman alpha emitters (LAEs) at $z = 6.6$ with a rather large scale length of ~ 12 kpc. The other detection comes from Kakuma et al. (2021) and Kikuchi et al. (2022) at 2σ significance at $z = 6.6$ also based on the stacking of narrowband imaging data. And while the James Webb Space Telescope (JWST) has recently opened the discovery space for Ly α observations towards $z \gtrsim 7$, it is not particularly sensitive to low surface brightness emission. This explains the absence of JWST-detected LAHs, with only one tentative sighting for the $z = 7$ galaxy DP7 (Pelliccia et al. 2021).

An obvious reason for the large absence of meaningful data of Ly α haloes at $z \geq 6$ is that such measurements are extremely difficult, due to the unfavourable combination of intrinsically very low surface brightness emission and cosmological surface brightness dimming. In this study we aim to improve on this situation by taking advantage of the MUSE eXtremely Deep Field (MXDF; Bacon et al. 2023), arguably the most sensitive observational dataset for such purposes in existence. We conduct a systematic search to detect extended Ly α emission around faint LAEs at $z \geq 6$ and measure the properties of such emission. We then compare these properties with those of LAHs at $z \sim 3$, taking great care to eliminate possible biases arising from redshift-dependent differences in the sensitivity to *intrinsic* surface brightness.

The paper is organized as follows: in Sect. 2 we introduce the data and the derived samples. Section 3 describes the construction of Ly α and UV continuum images as well as our LAH detection procedure. The parameters of individually detected LAHs are determined and characterised in Sect. 4. Section 5 is focused on spectral line properties of studied LAEs. We discuss the implications of our findings in Sect. 6 and conclude in Sect. 7. We use AB magnitudes throughout and express all distances in physical kpc. We assume a Λ CDM cosmology with $H_0 = 70$ km s $^{-1}$ Mpc $^{-1}$, $\Omega_m = 0.3$, and $\Omega_\Lambda = 0.7$.

2. Data and sample construction

Since our goal is to compare the properties of Ly α haloes at two very different redshift ranges, cosmological surface-brightness dimming is a major issue, with a factor ~ 10 loss in effective sensitivity between $z \sim 3$ and $z \sim 6$. The typical exponential scale length of a LAH with luminosity $L_{\text{Ly}\alpha} \sim 10^{42} L_\odot$ at $z = 3$ is only ~ 4 kpc (FL17), comparable to the size of the ground-based point spread function (PSF) even under good conditions. Observing a halo of the same intrinsic properties but at $z \geq 6$, using the same instrumental setup and depth, would lead to a $2\times$ smaller isophotal radius and complete noise dominance over any real extended emission at $\gtrsim 1-2$ scale lengths. These effects taken together could make all the difference for the detectability of Ly α haloes and must therefore be taken into account.

In the following we describe our approach to address this issue by comparing two samples at different redshifts that were extracted from observational data matched in intrinsic (i.e., corrected for cosmological dimming) surface brightness sensitivity. For both samples we use observations conducted with the Multi-Unit Spectroscopic Explorer (MUSE; Bacon et al. 2010) mounted on the ESO Very Large Telescope (VLT). MUSE is a panoramic integral field spectrograph with an instantaneous field of view of $1' \times 1'$ at $0''.2 \times 0''.2$ sampling and a wavelength range from 4700 Å to 9350 Å. The corresponding redshift range in Ly α is $z = 2.87$ to 6.67. One MUSE spectral pixel is 1.25 Å and the

spectral resolution is ~ 2.6 Å, depending weakly on wavelength. All MUSE datasets used in this study benefit from improved image quality from Ground-Layer Adaptive Optics (GLAO), resulting in a PSF full width at half maximum of typically better than $0''.5$.

2.1. High-redshift ($z \geq 6$) sample

We selected our high-redshift sample from the MUSE eXtremely Deep Field (MXDF, Bacon et al. 2023), a blind spectroscopic survey consisting of many exposures in a single pointing inside the Hubble Ultra Deep Field (HUDF). The MXDF has a coadded exposure time of 141 hours over a circular field of view of $1'$ in diameter and reaches a 3σ surface brightness limit of $\sim 1.0 \times 10^{-19}$ ergs $^{-1}$ cm $^{-2}$ arcsec $^{-2}$ in a $1'' \times 1''$ aperture for an unresolved emission line around 7300 Å. Our sample was drawn from the AMUSED catalogue and database by Bacon et al. (2023)¹, comprising altogether 2221 objects in the HUDF with spectroscopically measured redshifts. The location of the MXDF inside the HUDF implies that extensive space-based imaging data is also available (see Sect. 2.3).

We selected all galaxies in AMUSED with $z \geq 6$ falling within the MXDF footprint. We discarded one of these (AMUSED ID 8003) that was detected only in the shallower UDF-MOSAIC data, but not recovered in the MXDF datacube, implying it might be a noise spike rather than a real object. This left us with a set of 18 confirmed Ly α emitters. Their main properties are summarised in Table 1. Most of the sample lies in the high-exposure ($t_{\text{exp}} > 100^{\text{h}}$) area of the MXDF, with only 4 galaxies outside that region ($t_{\text{exp}} \approx 30^{\text{h}}$). The top left panel of Fig. 1 shows the spatial locations of these objects superimposed on the MXDF white-light image.

Since all galaxies in this sample are single-line detections, we have to ensure that their classification as high- z LAEs is robust and the sample is not contaminated by low-redshift interlopers. This is supported by several arguments: (i) As discussed in Sect. 5, the Ly α line is resolved for all objects and generally displays the characteristic skewed spectral profile, excluding the [O II] $\lambda\lambda 3727, 3729$ doublet as a possible contaminant and also arguing strongly against [O III] $\lambda 5007$ which for such faint galaxies is generally unresolved in MUSE. (ii) Most objects show detectable continuum counterparts in JWST F115W images but are undetected in the extremely deep HST F775W data, leading to photometric redshifts consistent with their spectroscopic z . (iii) Based on published luminosity functions of the relevant lines (Comparat et al. 2016), we expect that more than 90% of the single line emitters at wavelengths $\lambda > 8500$ Å and close to the MXDF flux limit are LAEs.

The redshifts of the objects are indicated by the red dashes in the bottom right corner of Fig. 2. Due to the strong impact of the terrestrial night sky background on the achievable sensitivity at wavelengths $\gtrsim 7000$ Å, the selected LAEs are typically found in narrow spectral windows in-between the atmospheric OH lines clearly visible in the variance spectrum. This leads to several of the Ly α lines being adjacent to high-variance regions which impacts the propagation of formal uncertainties and makes the estimation of realistic error bars a crucial part of the analysis.

To investigate the Ly α line spectral profiles, we re-extracted all LAE spectra from a continuum-subtracted datacube, with the continuum estimated by median filtering the original cube with a window of 151 pixels in dispersion direction, ensuring the removal of the stellar continuum of the galaxy itself as well as fore-

¹ <https://amused.univ-lyon1.fr/project/UDF/>

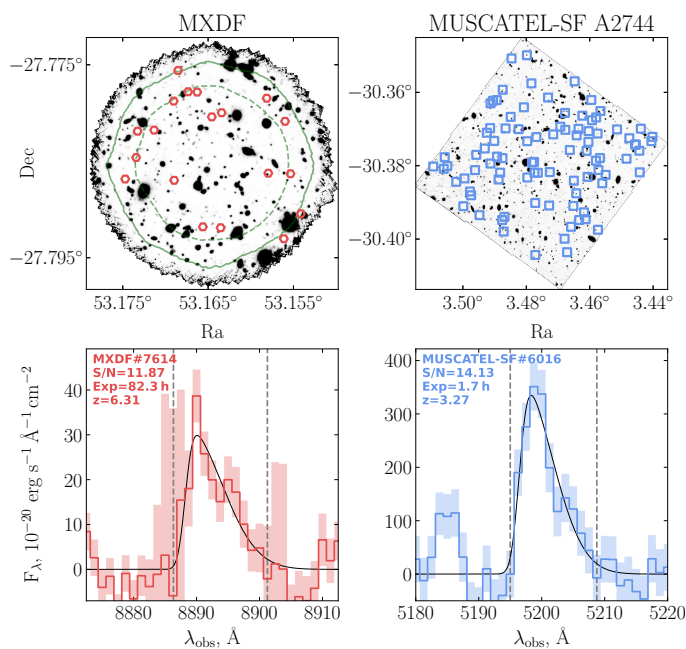


Fig. 1. *Top:* Spatial distribution of LAEs from high and lower redshift samples in their respective fields. The dashed and solid lines in the top left panel show the MXDF 30- and 140-hour exposure time iscontours. *Bottom:* Examples of Ly α spectra from both samples. The dashed vertical lines indicate the spectral bandwidth used to extract the pseudo-narrowband images used in the analysis. The thin black lines show skewed Gaussian fits to the observed line profiles.

and background objects. Spectra were extracted by summing the data over an aperture of $1''$ in radius. Overlapping foreground sources were masked to eliminate possible contamination from any intervening emission lines. In the bottom left panel of Fig. 1 we show an example Ly α spectral line profile displaying the characteristic skewed line shape.

2.2. Comparison sample at $z \sim 3.2$

We employed two main criteria to select our lower-redshift comparison sample. (i) It should feature a large difference in mean redshift from our $z \geq 6$ dataset, preferably in the range $3 \lesssim z \lesssim 4$ where LAH properties have been extensively studied. (ii) The observational data used for the comparison sample should have a similar *intrinsic* Ly α SB sensitivity as the MXDF data at $z \geq 6$, after accounting for cosmological dimming as well as for the (mild) variations of the MUSE instrument throughput with wavelength. Instead of degrading deeper exposures with artificial noise, which always introduces the danger of being too idealised, we searched our portfolio of MUSE surveys for a dataset with the appropriately matched quality. Besides the MXDF we considered the following surveys (numbers in parentheses indicating the mean exposure times): UDF-MOSAIC (10^h) and UDF-10 (31^h , Bacon et al. 2017, Bacon et al. 2023); MUSE-Wide (1^h , Urrutia et al. 2019); and the recent MUSCATEL MUSE Cosmic Assembly survey Targeting Extragalactic Legacy fields) survey (XXXXXXXX, in preparation; see also below) with three different depths, MUSCATEL-DF (25^h), -MF (5^h), and -SF (1.7^h).

To quantify the SB sensitivity at any given wavelength, we assumed it to be proportional to the so-called effective noise $\sigma_{\text{eff}}(\lambda)$ (Urrutia et al. 2019) which we routinely determine for each datacube in the postprocessing following the data reduc-

Table 1. Properties of the high- z LAE sample.

ID	z	$\log_{10}(L_{\text{Ly}\alpha}^{\text{CoG}} / [\text{erg s}^{-1}])$	M_{UV}
802	6.11	41.82 ± 0.19	-16.83 ± 0.15
852	6.64	42.05 ± 0.04	-18.69 ± 0.08
6332	6.33	41.90 ± 0.28	-16.41 ± 0.21
7610	6.10	42.11 ± 0.06	-17.71 ± 0.13
7614	6.31	42.08 ± 0.08	-18.96 ± 0.07
7692	6.31	41.68 ± 0.22	-18.09 ± 0.09
7699	6.64	42.06 ± 0.04	-19.46 ± 0.10
8145	6.04	41.48 ± 0.14	–
8172	6.00	41.47 ± 0.15	-15.33 ± 1.07
8179	6.60	41.46 ± 0.40	–
8209	6.57	40.93 ± 0.13	–
8211	6.00	41.36 ± 0.13	–
8214	6.63	41.70 ± 0.08	-18.63 ± 0.09
8367	6.58	41.15 ± 0.16	–
8379	6.63	41.45 ± 0.16	-16.63 ± 0.3
8384	6.05	41.13 ± 0.15	–
8433	6.55	41.17 ± 0.16	–
8461	6.49	41.46 ± 0.19	–

Notes. ID: source identifier in the AMUSED database. z : redshift determined from the Ly α line peak position. $\log_{10} L$: Ly α luminosities derived with the curve of growth method on the NB images. M_{UV} : rest-frame UV magnitude in the F115W filter of the associated UV counterpart from JADES if present.

tion (see also Weilbacher et al. (2020) for a comprehensive discussion of the noise properties of MUSE data). The effective noise is given in calibrated flux units per pixel and includes both the wavelength-dependent MUSE throughput and the co-added exposure level of the corresponding datacube, multiplied by an approximate correction for covariance losses due to correlated noise. To this we applied a $(1+z)^4$ modulation factor to account also for cosmological surface brightness dimming. We thus define the *intrinsic* Ly α SB sensitivity within a standard aperture of $1''$ as

$$\text{SB}_{\text{lim, Ly}\alpha}(\lambda) = \sigma_{\text{eff}}(\lambda) [z_{\text{Ly}\alpha}(\lambda) + 1]^4. \quad (1)$$

In Fig. 2 we compare the values of $\text{SB}_{\text{lim, Ly}\alpha}$ of typical MUSE cubes obtained in several of our ‘deep field’ spectroscopic surveys. As the abundance of skylines makes it difficult to easily estimate the sensitivity levels for $\lambda \geq 8000 \text{ \AA}$, a histogram of $\text{SB}_{\text{lim, Ly}\alpha}$ values for the high-redshift sample evaluated at the location of each object is plotted along the vertical axis on the left.

This figure suggests that LAEs at $z \sim 3\text{--}3.5$ from MUSCATEL-SF would provide the best match in $\text{SB}_{\text{lim, Ly}\alpha}$ to our ultradeep LAE sample at $z \geq 6$. The MUSCATEL project (PIs: L. Wisotzki, R. Bacon, T. Contini) is a recently concluded blind MUSE survey in the parallel fields of the Hubble Frontier Fields (HFF, Pagul et al. 2021, Lotz et al. 2017), focussing on regions near the clusters A2744, M0416, AS1063, and A370 – but sufficiently far from the cluster centres so that magnification effects due to cluster gravitational lensing are very small and for the present purpose negligible.

MUSCATEL encompasses three different levels of coadded exposure time: ‘‘Shallow fields’’ (SF) with $t_{\text{exp}} = 100^m$, ‘‘medium-deep’’ (MF) with $t_{\text{exp}} = 5^h$, and ‘‘deep’’ (DF) with

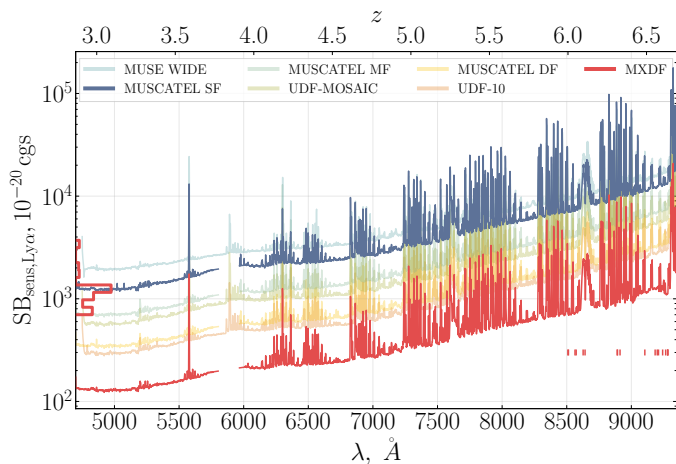


Fig. 2. Intrinsic (redshift-corrected) surface brightness sensitivity limit $SB_{\text{lim}, \text{Ly}\alpha}$ as a function of wavelength ($\text{Ly}\alpha$ redshift) for MUSE datacubes from different surveys as indicated in the legend (see text for references). The red horizontal histogram on the left shows the distribution of $SB_{\text{lim}, \text{Ly}\alpha}$ of our $z \geq 6$ sample, and the red dashes mark the observed $\text{Ly}\alpha$ wavelengths of the objects in that sample.

$t_{\text{exp}} = 25^{\text{h}}$. A full data release of datacubes and catalogues and an accompanying survey publication are in preparation. The MUSCATEL data set has also been described in Pessa et al. 2026, where the authors draw a sample of galaxies from the MUSCATEL survey to study their galactic outflow properties. In broad terms, the strategy for MUSCATEL has been similar to that adopted in previous MUSE surveys of the HUDF and surrounding regions. In particular, LAEs were selected as significant emission line peaks in the 3D datacubes using the matched-filter algorithm LSDCat (Herenz & Wisotzki 2017, Herenz 2023), followed by redshift (and redshift confidence) assignment by three independent human classifiers. For the present study we restricted ourselves to the ‘‘SF’’ subset in the parallel field to A2744, which provides data with the best seeing conditions among the MUSCATEL-SF observations. We initially selected all LAEs at $3 \leq z \leq 3.4$, of which we then removed two due to their close proximity to a bright galaxy or a star. This left us with 90 objects for the $z \sim 3$ comparison sample. We expect minimal contamination of the sample by the low-redshift line emitters (primarily $[\text{O II}]$ and $[\text{O III}]$) as they would have distinct spectral shapes, well-resolved stellar counterparts and are too few, given the survey volume at the relevant redshifts. See Bacon et al. (2015) and Bacon et al. (2023) for an extended discussion on redshift classification and potential low- z interlopers.

The spatial distribution of these sources over the MUSCATEL-SF A2744 footprint is shown in Fig. 1 alongside an example $\text{Ly}\alpha$ spectrum. The extraction of their spectra for this study was done in the same way as for the $z \geq 6$ MXDF sample, see Sect. 2.1.

2.3. Rest-frame UV data

In addition to the MUSE observations we used space-based imaging at rest-frame UV wavelengths to estimate the stellar continuum properties of the galaxies in our study. For the high-redshift sample we exploited the JWST Advanced Deep Extragalactic Survey (JADES Eisenstein et al. 2023, Bunker et al. 2024, D’Eugenio et al. 2025), which covers the entire footprint of the MXDF with 11 filters ranging from F090W to F444W. Among the available filters we chose the NIRCcam F115W filter

as it is free from $\text{Ly}\alpha$ contamination and provides the deepest observations in the rest-frame UV at $z \sim 6$. For the $z \sim 3$ sample in the MUSCATEL-SF A2744 field we employed HST/ACS observations from the HFF project (Shiple et al. 2018), selecting the ultradeep F814W band as the main reference for similar reasons. For each dataset we also consulted the associated source catalogue with photometric redshift estimates.

For each $\text{Ly}\alpha$ emitter in both samples we identified by visual inspection the most likely UV counterpart (in 11/18 objects of the MXDF and all of the MUSCATEL-SF sample), or decided that no such counterpart could be detected (7/18 and 0/90, respectively). For 8 objects in the lower-redshift sample and for 2 objects in the $z \geq 6$ sample we found a clear UV source (albeit rather faint, $m_{\text{F814W}}^{\text{lim}} = 29.1$ mag and $m_{\text{F115W}}^{\text{lim}} = 30.5$ mag) spatially coinciding with the $\text{Ly}\alpha$ emission, which however had no record in the corresponding published catalogue. In all those cases we assumed the uncatalogued UV source to be the counterpart. For 7 of the 18 high-redshift LAEs we deemed the angular and/or photometric redshift distances between LAE centroid and the closest UV source as too large (more than 5.5 kpc in all cases), so that no counterpart was assigned. For the $z \sim 3$ sample we encountered no such case. We found a mean offset of $0'':25$ between $\text{Ly}\alpha$ and UV centroids for both samples, only slightly more than one MUSE spaxel and in excellent agreement with previous measurements (Claeysens et al. 2022).

We used the available broadband photometric data also to estimate stellar masses (M_{\star}) and star formation rates (SFR) by fitting the spectral energy distributions (SEDs). As a baseline we employed the FAST code (Kriek et al. 2009) with models from the Bruzual & Charlot (2003) stellar library, assuming a Chabrier IMF (Chabrier 2003) and an exponentially declining star-formation history. FAST also estimates the dust attenuation acting on the starlight, assuming a Calzetti et al. (2000) extinction curve. We run the SED fitting routine using all available HST and JWST photometric data for all objects.

The choice of a specific star formation history (SFH) can significantly influence SED derived stellar mass and SFR by altering the mass-to-light ratio (e.g. Lower et al. 2020). To explore the effect of the adopted SFH on the estimated galaxy properties, we conducted the following study using Prospector. Prospector is a Bayesian forward-modelling code developed to derive the physical properties of galaxies from photometric or spectroscopic data using Markov chain Monte Carlo sampling. It uses FSPS stellar population models (Conroy et al. 2009, Conroy & Gunn 2010) with Chabrier IMF (Chabrier 2003), self-consistent nebular emission generated with Cloudy as described in Byler et al. (2017), and dust attenuation law with Calzetti et al. (2000) extinction curve as a default. The main advantage of Prospector is a very flexible treatment of SFHs: the built-in functions allow for various parametric models (such as τ and delayed- τ) and five non-parametric ones (continuity, continuity_flex, continuity_psb, dirichlet, and stochastic), which mainly vary in the resulting smoothness of the reconstructed SFH.

For our experiment, at both redshifts we selected 4 galaxies that uniformly probe the M_{UV} distribution in each sample. Then, we again estimated stellar masses and SFRs, now using Prospector assuming six different star formation histories: τ and delayed- τ , continuity, continuity_flex, dirichlet, and stochastic². We report that at $z \geq 6$ the stellar masses inferred assuming different star formation histories are generally

² We excluded the continuity_psb SFH prescription as it is tailored to galaxies in the post-starburst phase.

consistent with FAST results within ~ 0.3 dex. At $z \sim 3$ agreement between different codes and SFH treatments gets weaker and the difference increases to ~ 0.6 dex. This happens because we lack the photometric coverage redward of the Balmer break or even miss the break completely in $\sim 35\%$ of the objects due to the smaller F160W footprint. At both redshifts we recover rising SFHs for the nonparametric prescriptions and very low ages for the τ models, indicating active star formation in these galaxies at the time of observation. From this experiment we conclude that derived stellar masses and SFRs are fairly robust against variations in the star formation histories given the available data.

3. Detection of Ly α haloes

In order to study individual Ly α haloes we need to distinguish between objects with and without significantly detected extended emission. In accordance with most previous work (e.g., LW16, FL17) we base this decision on a comparison with the spatial extent of the stellar light distribution: If the SB distribution of the Ly α emission is consistent with the distribution of starlight (within the error bars and after accounting for PSF blurring) we adopt the null hypothesis that the observed Ly α emission originates mainly in the ISM of the host galaxy, with no evidence for a circumgalactic component due to scattered light or added emission. Only if this null hypothesis is significantly rejected do we take the Ly α halo as detected. As in our previous LAH studies using MUSE (e.g. LW16 and FL17), a key ingredient to this test are the deep high-resolution space-based images available in our fields, allowing us to constrain the stellar light distribution much more accurately than possible from the MUSE data alone.

3.1. Image construction

3.1.1. Ly α pseudo-narrowband images

For each object we extracted a $6'' \times 6'' \times 6''$ (33×33 MUSE spaxels) pseudo-narrowband (NB) image from the corresponding MUSE datacube. The image size was chosen so that we could detect and model the extended Ly α emission of all objects of interest while limiting the impact of nearby sources. We used the median filter subtracted cubes (see LW16 for details) to approximately remove the continuum of target galaxies and back-/foreground sources.

The size of each narrowband was chosen manually to incorporate most (but not strictly all) of the Ly α flux in the band (see example in Fig. 1). Since the blue peaks of Ly α emission lines are increasingly lost to IGM absorption towards high redshifts (e.g., Mason & Gronke 2020, Hayes et al. 2021) we treated our $z \sim 3.2$ objects similarly and deliberately excluded any blue peak emission also in those. The resulting typical NB width for both samples was 9 MUSE spectral pixels (11.25 \AA). Examples of constructed Ly α pseudo-narrowband images are shown in the left column of Fig. 3.

3.1.2. UV continuum images and model fits

A typical Ly α emitter detected in MUSE is a low-mass star-forming galaxy identified by its bright emission line, but with a very faint and often tiny continuum counterpart. Using the deepest available reference images (see Sect. 2.3) we extracted matching $6'' \times 6'' \times 6''$ cutouts (220×220 pixels at the $0''03$ sampling of the HST and JWST data). All sources except the assigned UV counterpart were masked. We used GALFIT

(Peng et al. 2002, 2010) to model each object as a linear combination of standard functions (point source, exponential, Sérsic profile) convolved with the PSF. For the MXDF sample we used a simulated JWST NIRCcam PSF from the JWST PSF simulation library³. For the HST data of the MUSCATEL sample we assumed a symmetric Gaussian PSF with FWHM adopted from Shipley et al. (2018). Single component models were sufficient to fit the UV counterpart of all the $z \geq 6$ objects. Of the lower redshift sample 61/90 objects could be modelled with just one component, 20 required two, 7 were modelled as three- and 2 as four-component systems. The 7 high- z objects undetected in the continuum were treated as point sources in the remaining analysis. Second and third columns of Fig. 3 show examples of the UV continuum images and models after resampling to MUSE resolution and convolving with the MUSE PSF.

3.2. Detection procedure

We now describe our LAH detection test procedure. In contrast to previous studies, our null hypothesis test for the presence of extended Ly α emission is based on a spaxel-to-spaxel evaluation of the light distribution, combined with an empirical self-calibration of the noise properties using empty regions. For each object we performed the following steps:

1. We determined the centroid and flux scaling amplitude of the resampled and convolved UV continuum model to best match the Ly α NB data. For the centroid we fitted the NB image with a 2D Gaussian using the photutils package (Bradley et al. 2025). We then calculated the scaling factor for the continuum model placed at this location by χ^2 minimisation and record the corresponding value of χ^2 .
2. Next we defined a list of empty fields in the NB image of the full datacube. To do so we first smoothed the image with a Gaussian kernel with σ of 1.5 pixels and constructed a binary mask to hide extended sources. Recall that the NB images were already continuum-subtracted using the prior median-filtered datacube, so this masking step mainly marked emission line sources (in particular by foreground [O II] emitters), but also cases of poor continuum subtraction. We projected a rectangular grid with a spacing of 16 pixels onto the image, and at each location we tested if a small ($3''3 \times 3''3$) NB image centred on this position intersected with the mask. Only if there was no such intersection did we record the location as an empty region. The resulting number of empty regions per object was around 300 in the MXDF and between 1500 and 2000 in the MUSCATEL-SF footprint.
3. To perform the null hypothesis test, we required a robust estimate of the noise inside each of the investigated apertures. While the “effective noise” approach (Urrutia et al. 2019) provides a good approximation for large-aperture measurements, it overestimates the noise level for the spaxel-by-spaxel comparison within small apertures around our LAEs. We therefore self-calibrated the goodness-of-fit test by the following iteration over the grid of empty regions, object by object: We inserted a copy of the UV continuum model scaled to the observed Ly α flux at each grid point and then re-determined the best centroid and matching scale factor as described above. After that we subtracted the scaled UV model from this mock field. Combining the residuals in a single empty region provided a χ^2 value (note that the noise level for faint objects in MUSE is entirely dominated by the background with a minor contribution of detector readout noise;

³ <https://stsci.app.box.com/v/jwst-simulated-psf-library>

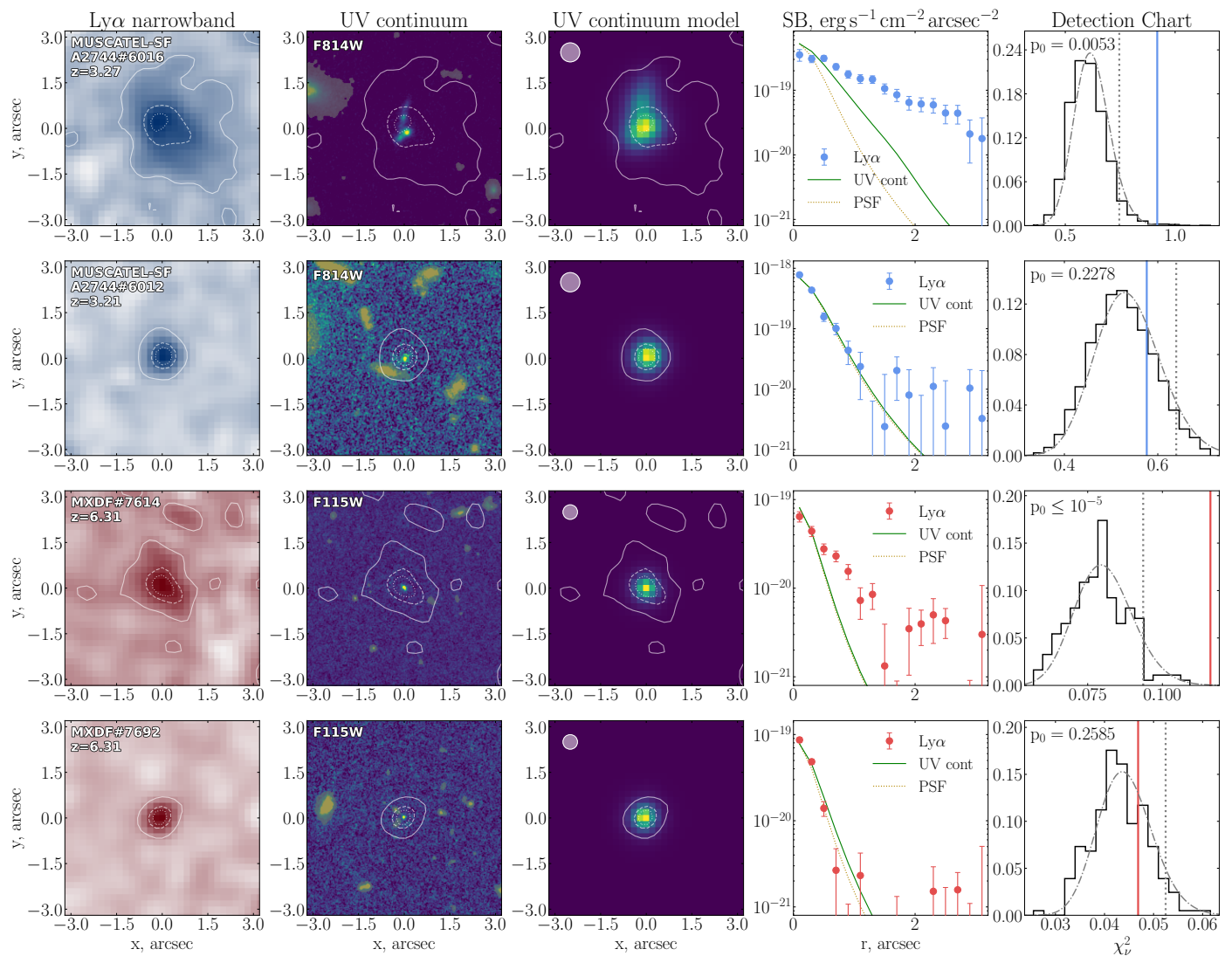


Fig. 3. Examples of LAEs in our sample. The upper two rows show objects at $z \approx 3.2$ subset from MUSCATEL-SF, the lower rows show $z \geq 6$ LAEs in the MXDF. Objects in the first and third rows are examples of clear Ly α halo detections. *First column:* Ly α narrowband images (smoothed for display purposes), with overlaid $SB \times (1+z)^4$ contours of 10^{-15} (solid), $2 \cdot 10^{-15}$ (dashed) and $2.5 \cdot 10^{-15}$ (dotted) $\text{erg s}^{-1} \text{cm}^{-2} \text{arcsec}^{-2}$. *Second column:* UV continuum images from either HST or JWST, with the filter specified in the top left corner. The overlay contours are the same as in the first column. *Third column:* GALFIT model of the UV continuum image resampled and convolved to MUSE resolution. The circle in the top left corner of each panel indicates the FWHM of MUSE PSF at the Ly α observed wavelength of each object. *Fourth column:* Azimuthally averaged SB profile of the Ly α emission (datapoints with error bars) compared to the UV continuum model fit (solid line) and to the PSF (dotted line). *Fifth column:* Distribution of reduced χ^2_ν values obtained in empty fields after inserting the “true” UV continuum model and then subtracting a flux-matched one. The thick vertical line shows χ^2_ν obtained for the object itself after subtracting the flux-matched UV continuum model. The probability p_0 of the null hypothesis (Ly α consistent with UV) is shown in the top left. The dotted line marks the χ^2_ν threshold corresponding to $p_0 = 0.05$. The dash-dotted line shows the χ^2 distribution fitted to the histogram.

shot noise from the object is negligible). For each object the histogram of χ^2 values of all inserted sources in the empty regions then resulted in the expected χ^2 distribution for the null hypothesis that the Ly α light distribution follows the UV. This procedure fully includes the errors from centroiding uncertainties, continuum subtraction artefacts, and sky subtraction residuals leading to imperfect flatfielding (particularly relevant at $z \geq 6$ where Ly α is observed between the multiplets of the OH night sky emission forest). We also made sure to account for variations in the received exposure time with location, again mainly relevant for the MXDF with its steep exposure gradient outside the $1' \times 1'$ circular area (Bacon et al. 2023).

4. As the last step we assessed for each object whether the Ly α spatial distribution is statistically distinguishable from the UV continuum model by determining the location of the measured χ^2 value of the object relative to the self-calibrated cumulative χ^2 distribution, expressed as a normalised frequency p . As in most previous studies we adopted a value of $p < p_0 = 0.05$ as the threshold for detecting extended emission; but now this threshold does not refer to a standard χ^2 test but to the actually measured distribution of residuals. In Fig. 3 we show examples for these χ^2 histograms together with the observed value of the object itself. From the fact that these histograms peak at χ^2 values well below unity it can be seen that the effective noise indeed overestimates the pixel uncertainties, implying that our self-calibration proce-

ture is both more realistic and more sensitive to detect faint Ly α haloes than previous approaches.

3.3. Results

3.3.1. Radial profiles

To visualise the spatial distribution of Ly α emission, we extracted azimuthally averaged surface brightness profiles in concentric circular annuli for the objects in our sample. Our annuli have radial increments of 1 MUSE pixel (0".2) to properly sample the inner LAH regions which are strongly affected by PSF blurring. Taking advantage of the procedure outlined in Sect. 3.2, we also estimated self-calibrated error bars for the SB profiles by constructing SB profiles of the empty fields using the same annuli and calculated the interquartile range (IQR) of all profiles in each radial bin. The values of IQR/1.34 were then adopted as 1σ uncertainty at each radius. We used the IQR statistic rather than standard deviations as uncertainty estimator because of its greater robustness against outliers. The thus derived error bars are typically $1.2\text{--}1.7 \times$ smaller than the ones formally propagated from the effective variances, but for objects located near strong sky emission lines (relevant for several of the $z \geq 6$ objects) this ratio increases up to 5.

3.3.2. LAH detection fractions

Before the final assessment of which objects have significantly detected LAHs we performed a visual inspection of all Ly α NB images and SB profiles to check for the integrity of the formal detections. We found and discarded four $z \sim 3.2$ objects with high relative χ^2 values which however appeared to be driven by sky or continuum subtraction residuals. After this last cleaning step we count 40/90 ($(44 \pm 5)\%$) detected LAHs at $z \sim 3.2$ and 6/18 ($(33 \pm 11)\%$) at $z \geq 6$. As our study was designed to compensate for cosmological SB dimming, we a priori expect that the detection rate should depend mainly on the intrinsic prominence of LAHs in these two redshift domains. The fact that the LAH fractions are not statistically significantly different might be taken as indication that also the typical LAH properties are similar. We demonstrate in Sect. 4 below that this is however not the case.

At face value our LAH detection rates are much lower than the $\sim 80\%$ reported in LW16 and FL17. For the redshift $z \sim 3.2$ comparison sample this can be easily explained by the reduced sensitivity of our current data compared to the much deeper exposures used for those studies. FL17 demonstrated in their Appendix how a factor 3 in exposure time already makes a big difference for measuring LAH properties. Our MUSCATEL-SF data have a $6\times$ shorter exposure time than the UDF-Mosaic and $20\times$ shorter than the UDF-10 and HDFS used by FL17 and LW16. Our stacking analysis (see Sect. 4.3) indeed demonstrates that the non-detections among our $z \sim 3.2$ objects typically have perfectly normal extended LAHs, which are just a little bit too faint to be detected individually at the sensitivity of the MUSCATEL shallow fields.

For our high redshift sample the comparison to LW16 and FL17 is not so easy to perform. On the one hand the effects of cosmological dimming make the intrinsic SB sensitivity (see Fig. 2) of the MXDF at $z \geq 6$ lower than that of the UDF-10 at $z < 5.5$ and of the UDF-Mosaic at $z < 4$, implying that a somewhat lower detection fraction should be expected. On the other hand, there could also be real differences in the properties of LAHs at these highest redshifts. In the following we show that a

more detailed comparison of the LAH properties in our two samples, including a stacking analysis, strongly suggests that this is indeed so, and that even deeper data than the MXDF would probably not result in a much higher LAH detection rate at $z \geq 6$.

4. Ly α halo properties

4.1. Surface brightness profiles and modelling

We now proceed to determine the main properties of our detected LAHs. In line with previous LAH studies (LW16, FL17) we approximate the Ly α emission as the sum of a central component that follows the spatial distribution of the stellar UV continuum and an extended halo component that is usually well described by an exponential surface brightness profile.

For the central component models we adopted our HST- and JWST-based UV continuum fits from Sect. 3.1.2. For each object we reconstructed the stellar light distribution in the UV, convolved with the MUSE PSF at the corresponding wavelength, keeping all parameters fixed except for the total Ly α flux of the component (F_c). The halo component was taken as a single exponential with four parameters: scale length ($r_{s,H}$), axis ratio (q_H), position angle (PA) and the total flux (F_H). To fit the model to the Ly α NB images, we again used GALFIT, with the additional constraint of forcing both components to have the same centroid. The fit was performed within a circular aperture of 10–14 pixels in radius, depending somewhat on the extent of the halo, plus a mask to avoid projected contaminating objects if required. For 6 LAHs in the $z \sim 3$ sample we had to force circularity of the halo for the fit to converge. In the case of the $z \geq 6$ objects, all halo fits converged with q kept free (but recall that only 6/18 objects show a detectable LAH). From these fits we calculated the halo flux fractions, $f_H = F_H/(F_H + F_c)$.

Fig. 4 compares the main halo properties of the $z \sim 3$ and $z \geq 6$ samples. Evidently, the two sets of objects have very similar distributions of f_H and q_H ; a Kolmogorov-Smirnov test gives p values of 0.98 and 0.64 that both are drawn from the same parent distribution. (See Appendix Fig. B.1 for a version of the left plot that includes upper limits for the individually undetected LAHs). There is a slight excess of relatively dim LAHs ($f_H \lesssim 0.5$) in the $z \sim 3$ sample, which comes primarily from objects where halo circularity was forced, indicating a potentially unreliable fit. On the other hand, Fig. 4 reveals a clear difference in the resulting halo scale lengths between the two samples: The LAHs at high redshifts are much more compact than their $z \sim 3$ counterparts, with the latter having typical scale lengths ~ 3 times larger than the former. Moreover, 39 out of 40 $z \sim 3$ LAHs have scale lengths larger than the mean (or median) of the $z \geq 6$ objects in the MXDF halo, and 29/40 are more extended than any of the high-redshift haloes.

Comparing our lower redshift measurements with the results of LW16 and FL17 – obtained with much deeper data – we find that the recovered distributions of LAH properties at $z \sim 3$ are in full agreement (see also Fig. 8 below). Our median halo scale length for the MUSCATEL sample is 5.3 ± 1.8 kpc (with the error bar representing the standard uncertainty of the median), while that value is 4.7 ± 0.6 kpc in the LW16 and 4.2 ± 1.5 kpc in the FL17 samples, for the same redshift interval $3 < z < 3.4$. These values are statistically consistent with each other, although slightly higher in our data. That is, however, naturally explained by the lower sensitivity of MUSCATEL-Shallow, meaning that the detected LAHs have higher Ly α luminosities, a property known to correlate with the haloes' scale lengths (FL17, Guo et al. 2024b, McKay et al. 2026). We obtain

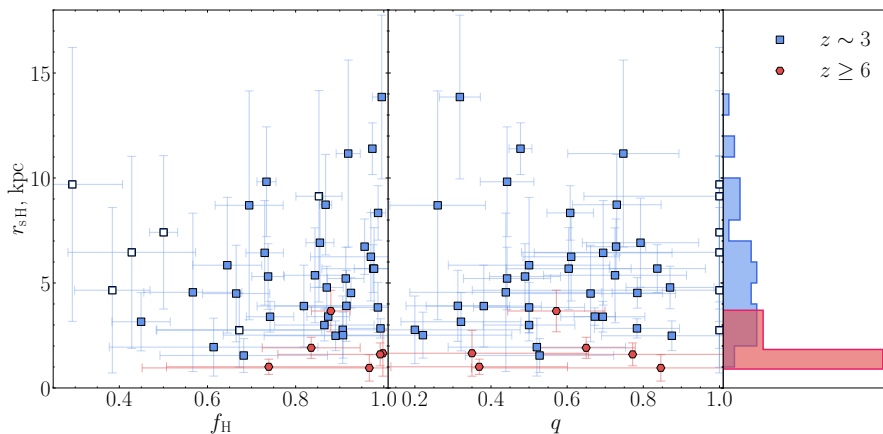


Fig. 4. Comparison of main LAH parameters for the $z \sim 3$ and $z \geq 6$ samples. The $z \sim 3$ objects are shown as blue squares, the $z \geq 6$ objects as red hexagons. The open markers indicate objects where the halo was forced to be circular in the fit. In the left panel we plot halo scale lengths against halo flux fractions, in the middle panel against halo axis ratios. The right panel shows the marginalised histograms of our fitted halo scale lengths, with the same colour coding as before.

a distribution of halo to continuum scale length ratios for our $z \sim 3$ sample which is also very similar to that seen by LW16 and FL17, with a median value of ~ 10 but a large scatter.

For our $z \geq 6$ sample there are almost no comparison data in the literature (see Introduction). The scale lengths of the only individually studied high- z LAHs (CR7 (Matthee et al. 2020a), VR7 (Matthee et al. 2020b) and z70-1 (Zhang et al. 2020)) are relatively close to our measured values, although it should be kept in mind that these objects are much more luminous (in Ly α as well as in UV magnitude) than our mostly very faint LAEs. 4 of the 6 $z \geq 6$ LAEs with detected haloes have identified UV counterparts in JWST, all of which are resolved beyond a point source. The ratios of their Ly α to UV scale lengths range between 1.7 and 16 with a median of 6.8, which given the small sample, is fully compatible with the observed relation for lower redshift LAEs.

4.2. Characteristics of Ly α haloes at $z \geq 6$

The six spatially resolved LAHs in our high-redshift sample more than double the number of known individual LAH detections around star-forming galaxies at $z > 6$. We present them in Fig. 5 and give their main structural parameters in Table 2. In the following we briefly comment on each source separately, in order of increasing redshift:

- MXDF#8211 ($z = 6.00$) has the lowest Ly α luminosity among all known LAHs to date. It shows no continuum counterpart in any of the available deep JWST images, implying a high Ly α equivalent width suggestive of a very metal-poor stellar population, a dust-free interstellar medium, and/or possibly contributions from other power sources than central photoionization (e.g., Cullen et al. 2020, Saxena et al. 2023).
- MXDF#8145 ($z = 6.04$) is located at the edge of the MXDF footprint and therefore has a significantly lower signal-to-noise ratio. In fact, a 1D SB profile test would have classified this object as not extended despite it showing clear signs of extended emission. Our self-calibrated 2D test reveals a Ly α halo around this source ($p_0 = 0.03$). It also shows no detectable counterpart in JWST. Notably, our image modelling with GALFIT prefers a single exponential with no separate central component.
- MXDF#7610 ($z = 6.09$) has a very similar Ly α scale length as VR7 (Matthee et al. 2020b), but at a $\sim 40\times$ lower Ly α luminosity. The UV counterpart of VR7 is even $\sim 300\times$ brighter and $2.4\times$ more extended than that of MXDF#7610. This highlights the diversity of the relation between galaxy and LAH properties. The inferred stellar metallicity of

the UV counterpart (both with FAST and Prospector) is amongst the lowest in the $z \geq 6$ sample.

- MXDF#7614 ($z = 6.31$) is located at the edge of the MXDF full exposure region, and its redshift places the Ly α line very close in wavelength to a night sky emission line. Due to these restrictions the halo is only detected with our self-calibration method. The halo is notably elongated. This is the most extreme high- z halo detected in the study. It is very similar to CR7 in terms of both line width and halo size (but not the Ly α luminosity). Moreover, this object is the only $z \geq 6$ LAH similar to the average $z \sim 3$ halo in the MUSCATEL sample. This is the only object in our $z \geq 6$ sample with available rest-frame spectroscopy from the JADES DR4 (Curtis-Lake et al. 2026, Scholtz et al. 2026). This means we can measure its Ly α velocity offset from systemic redshift $\Delta v_{\text{Ly}\alpha} = c(z_{\text{Ly}\alpha} - z_{\text{sys}})/(1 + z_{\text{sys}})$, where $z_{\text{Ly}\alpha}$ is the redshift estimated from the Ly α peak position, and z_{sys} – from rest-optical non resonant lines. We obtain the value of $220 \pm 55 \text{ km s}^{-1}$. Assuming Case-B recombination we calculate the Ly α escape fraction ($f_{\text{esc}}^{\text{Ly}\alpha} = F_{\text{Ly}\alpha} / 8.7 \cdot F_{\text{H}\alpha}$) to be ≈ 0.3 . Both values are typical, given object’s redshift and UV magnitude (e.g., Saxena et al. 2024, Tang et al. 2024, Chen et al. 2024).
- MXDF#7699 ($z = 6.63$) has the most compact halo detected in our sample despite being one of the most luminous objects. With a scale length of 1.2 kpc it is only marginally resolved, helped by the small error bars due to its relative brightness. The UV counterpart resembles an elongated U-warped edge-on galaxy, making the Ly α to UV size ratio one of the lowest recorded.
- MXDF#8214 ($z = 6.63$) is our highest redshift detected LAH. The NB image suggests a second emission source $\sim 2''$ away, which was however masked and therefore did not influence the Ly α halo detection (indicated by the grey band in the rightmost panel of Fig. 5). The secondary source is too faint for an independent classification, but if it is Ly α , then it would have a velocity offset of $\lesssim 300 \text{ km s}^{-1}$ from MXDF#8214. It also has a weak JWST counterpart with $z_{\text{phot}} = 6.590^{+1.459}_{-0.366}$, making it quite likely that this is a close companion at a projected distance of $\sim 12 \text{ kpc}$. The extended LAH of MXDF#8214 may thus be enhanced by gravitational interaction with its companion.

4.3. Stacking analysis

The vast difference in LAH scale lengths between $z \sim 3$ and $z \geq 6$ reported in Sect. 4.1 is necessarily based on only those ob-

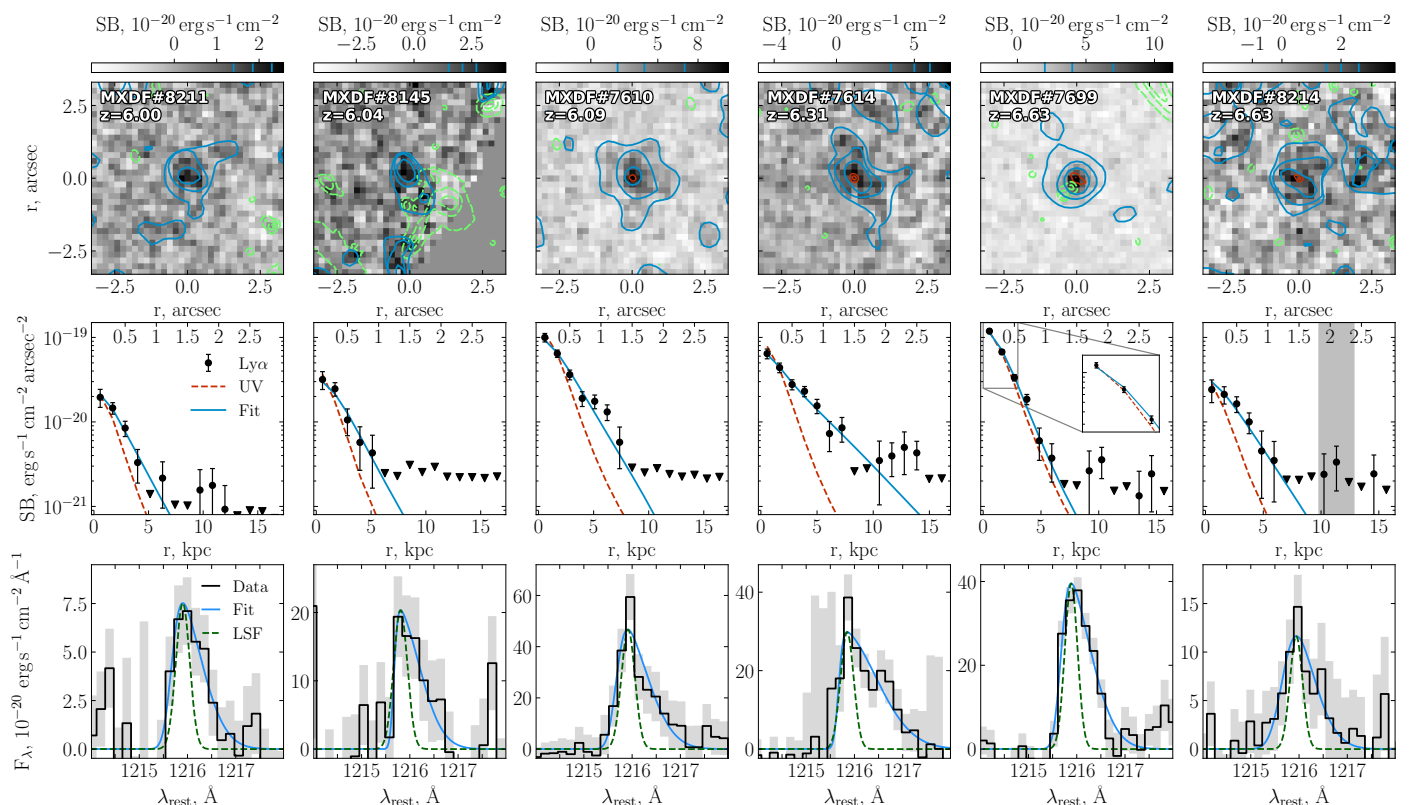


Fig. 5. Gallery of the six individually detected $z \geq 6$ Ly α haloes. *Top row:* Ly α narrow band images overlaid with smoothed SB contours (solid blue line) outlining emission from the core and the extended halo with values indicated in the color bar on top. Red contours show the F115W images of the assigned UV counterparts at JWST resolution (their absence indicates no counterpart). Fore- and background objects from same F115W image are shown in green dashed contours. AMUSED database ID and measured redshift are shown in the top left corner. *Middle row:* SB profile of observed Ly α emission (circles), scaled UV continuum model (dashed line) and the continuum + halo model 2D fit (solid line). 1 σ upper limits are shown with triangles. The three inner bins for MXDF#7699 are shown in the inset on a large scale. The grey band at 12 kpc (2'') in the last column shows SB enhancement associated with a potential companion of MXDF#8214. *Bottom row:* observed Ly α spectra (black step line with grey band), skewed gaussian fit to the data (blue solid) and MUSE LSF (green dashed).

Table 2. Summary of measured $z > 6$ Ly α halo and continuum quantities.

ID	$r_{s,c}$ [kpc]	q_c	$r_{s,H}$ [kpc]	q_H	f_H
8211 ^a	-	-	1.57 ± 1.10	0.78 ± 0.48	0.72 ± 0.20
8145 ^a	-	-	1.65 ± 1.09	0.35 ± 0.31	0.99 ± 0.24
7610	0.33 ± 0.04	0.65 ± 0.08	1.91 ± 0.50	0.65 ± 0.13	0.84 ± 0.11
7614	0.23 ± 0.01	0.57 ± 0.02	3.66 ± 0.99	0.57 ± 0.13	0.88 ± 0.04
8214	0.20 ± 0.02	0.51 ± 0.06	1.60 ± 0.55	0.77 ± 0.25	0.99 ± 0.23
7699	0.59 ± 0.03	0.23 ± 0.01	1.18 ± 0.36	0.37 ± 0.23	0.74 ± 0.23
Halo Stack	0.28 ± 0.01^b	0.47 ± 0.01	1.52 ± 0.21	0.65 ± 0.07	0.99 ± 0.02
Full Stack	0.23 ± 0.01^b	0.26 ± 0.02	1.27 ± 0.44	0.54 ± 0.14	0.55 ± 0.09

Notes. ID: source identifier in the AMUSED database. $r_{s,c}$: UV continuum scale length (if available). q_c : axis ratio of the UV continuum source. $r_{s,H}$: Ly α halo scale length. q_H : halo axis ratio. f_H : Ly α halo flux fraction. ^(a) No counterpart detected, central component modelled as point source. ^(b) Values converted from Sérsic half-light radii.

jects where we could significantly detect an extended halo. Since LAH detectability depends strongly on the quality of the data, in particular depth and angular resolution, a non-detection by no means implies the absence of an extended halo. In Appendix B we address this point by estimating upper limits on the halo flux fractions and the halo scale lengths for all our undetected LAHs.

A popular approach to increase the depth of imaging data, at least in a statistical sense, is stacking. We therefore stacked the Ly α narrowband images of all LAEs where no individual halo

could be detected, separately for each sample. From the centroid-aligned NB images with their associated variance maps and UV continuum model images we obtained pixel-by-pixel median and mean Ly α and UV continuum images. We then extracted azimuthally averaged SB profiles from the stacked images and again performed a null hypothesis test for consistency between UV and Ly α profile. Since our 2D self-calibration method could obviously not be applied here, we reverted to the simpler 1D profile test already adopted by LW16.

Fig. 6 contrasts the resulting median-stacked Ly α SB profiles for the two samples. For this comparison we scaled the SB values of the $z \geq 6$ stack by a factor of 9.12 to their equivalent values at redshift $z = 3.2$ (the median redshift of the MUSCATEL sample), thus approximately correcting for cosmological SB dimming. More details on the stacking results that include also the detected LAH objects are provided in Appendix A.

Remarkably, for the high-redshift undetected LAH sample, neither the mean nor the median stack shows any indication that the Ly α SB profile differs significantly from the UV continuum profile, given the variance-propagated uncertainties. As discussed in Appendix B, this implies a halo flux fraction of less than 0.4 and/or a very compact stacked halo with $r_{s,H} \lesssim 1.3$ kpc.

In sharp contrast, the $z \sim 3$ stack of the objects with individually undetected LAHs reveals highly significant Ly α emission extending out to more than 10 kpc, with a SB profile very different from the stacked UV continuum. This strongly confirms the notion that most non-detections at $z \sim 3$ are “narrow misses” that in only slightly deeper data would have been recognized as individual LAHs. To measure the scale length, we first fitted the UV continuum stack with a Sérsic profile. We then used this continuum model with fixed shape parameters plus an exponential profile to describe the extended halo. The resulting Ly α scale length is 6.84 ± 1.26 kpc for the median and 7.84 ± 1.23 kpc for the mean stack, respectively.

The difference between the two samples is striking. We reiterate that the intrinsic (de-redshifted) SB sensitivities of MUSCATEL-Shallow at $z \sim 3$ and of the MXDF at $z \geq 6$ are essentially the same. The error bars of the $z \geq 6$ stacked profiles are larger only because of the smaller number of objects in the high-redshift sample. The difference in the number of stacked objects is also inadequate to explain this result: stacking only 12 of the 50 $z \sim 3$ LAEs would increase the individual error bars by a factor of ≈ 2 , which is clearly insufficient to make the $z \sim 3$ Ly α SB profile consistent with the UV continuum profile. We thus conclude that Ly α haloes of LAEs at $z \geq 6$ are either generally much smaller and fainter than those at lower redshifts, or that a large fraction of LAEs at $z \geq 6$ is even entirely devoid of any Ly α halo.

5. Spectral properties

To gain deeper insight into the physical origin of the observed halo differences, we investigated the Ly α emission line spectra of the galaxies in each sample, since the Ly α line profile is known to correlate with Ly α halo properties, both from a theoretical perspective (Verhamme et al. 2006, Gronke 2017) and empirically (FL17, Leclercq et al. 2020). We fitted the red peak (the blue peak of $z \sim 3$ LAEs was excluded to maintain consistency with the high- z sample) of each Ly α emission line with a “skewed Gaussian” profile (Bacon et al. 2023), convolved with a Gaussian representing the MUSE line spread function (LSF) at line centre, using non-linear least-squares. The obtained Ly α line widths (defined as the full width at half maximum, FWHM) are therefore approximate intrinsic widths with the instrumental broadening removed.

Figure 7 compares the line width distributions of the LAEs in our two samples. Most of the lines at both high and low redshift are resolved, although some of them only marginally. Only $\sim 20\%$ of the FWHM values fall below the LSF resolution, implying that their widths cannot be adequately constrained. The figure also shows the FWHM distributions for only the objects with individually detected haloes. We confirm the known trend

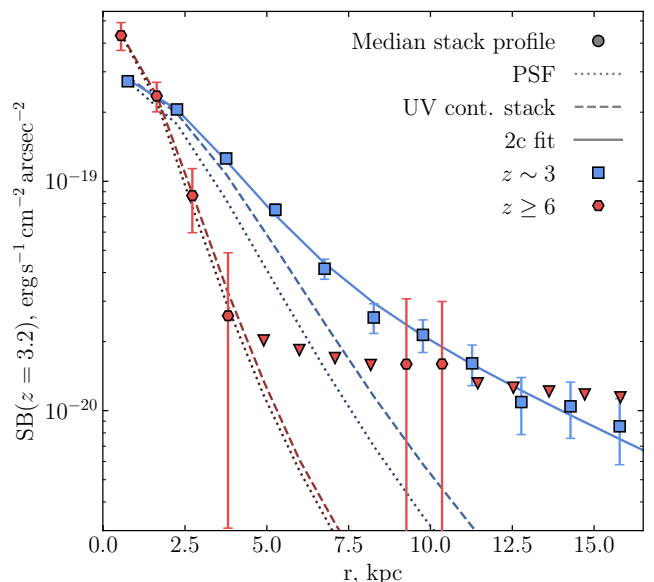


Fig. 6. Median-stacked Ly α surface brightness profiles of our LAEs with undetected Ly α haloes. The blue squares represent the $z \sim 3$ sample, red hexagons the $z \geq 6$ sample. The latter values are corrected for cosmological dimming, such that the ordinate refers to surface brightnesses at $z = 3.2$. 1σ upper limits are shown with triangles. The profiles of the PSF and of the UV continuum stacks are shown in dotted and dashed lines, respectively. The blue solid line represents the profile of a 2-component fit to the $z \sim 3$ stacked images.

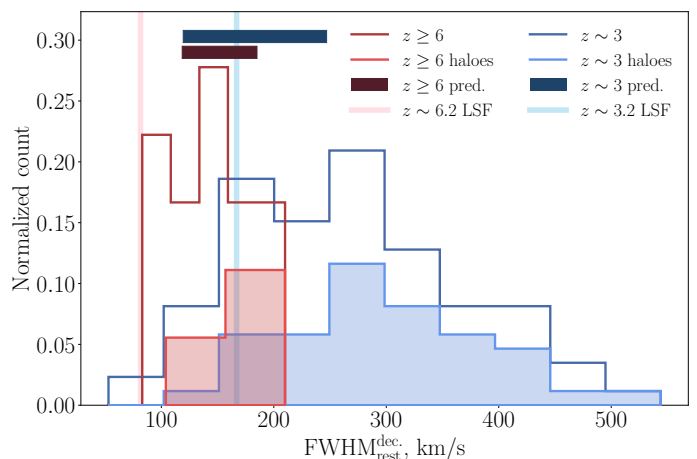


Fig. 7. Distribution of Ly α line widths (FWHM) for both samples, after deconvolving by the MUSE LSF. The open red and blue histograms give the results for the $z \geq 6$ MXDF and the MUSCATEL $z \sim 3$ samples, respectively. The filled red and blue histograms show this distribution for only LAEs with detected haloes at $z \geq 6$ and $z \sim 3$ respectively. The vertical lines indicate roughly the MUSE spectral resolution, for both samples. The horizontal bars at the top outline the range of expected intrinsic virial line widths from a simple stellar mass–halo mass conversion.

(FL17) that objects with significantly detected LAHs tend to exhibit larger line widths, for both samples.

As is the case for the halo scale lengths, the distributions of line widths differ substantially between the two samples, with more than half of the lower- z LAEs having lines broader than any of the $z \geq 6$ objects. On the other hand, the skewness parameters of the line profile are very similar with a mean of $\gamma \approx 9$ for both samples. This could however be a consequence of two effects

conspiring. The skewed profile of Ly α is usually believed to be a direct consequence of resonant scattering and photon escape through an optically thick, kinematically complex interstellar and circumgalactic medium of galaxies (e.g., Verhamme et al. 2006, Blaizot et al. 2023). However, at high redshifts the line is further driven towards asymmetry by the evolving Ly α forest opacity and the subsequently developing damping wing of intergalactic H I absorption (Mason & Gronke 2020). The impact of this second effect on the resulting profile shape depends strongly on the offset of the Ly α peak from the systemic redshift, which in turn depends on the internal gas column density and kinematics. At the redshift range of our MXDF sample ($6 < z < 6.7$) we expect mainly a sharp cutoff at z_{sys} , but not yet a substantial IGM damping wing. If the Ly α peak offsets in our sample are around 200 km s^{-1} , similar to those observed for lower redshift LAEs (Verhamme et al. 2018, Muzahid et al. 2020, Schmidt et al. 2021), then the alteration of the profiles should be relatively modest, and it would be implausible to invoke IGM absorption to explain the observed lower FWHM values in our high- z sample. We conclude that the differences in Ly α line widths are most likely real and reflecting intrinsic differences in the properties of the sources.

We now explore whether these differences might be caused by systematically higher dynamical masses of LAH host galaxies at $z \sim 3.2$, leading to higher velocity dispersions and correspondingly broader lines already before any scattering. To estimate the expected line broadening from the halo gas velocity dispersion, we first converted the stellar masses of all galaxies with detected HST or JWST counterparts into rough halo mass estimates using the stellar mass–halo mass relation from Behroozi et al. (2013). We estimated the one-dimensional velocity dispersion via the virial theorem using the calibration from Evrard et al. (2008) as

$$\sigma_{1D} = 1082.8 \left[\frac{h(z) M_h}{10^{15} M_\odot} \right]^{1/3} \text{ km s}^{-1}, \quad (2)$$

where M_h is the halo mass and $h(z)$ is the dimensionless Hubble parameter at redshift z . Finally, the velocity dispersion σ_{1D} was multiplied by 2.355 to obtain the predicted line width $\text{FWHM}_{\text{pred}}$. Figure 7 represents the 16th–84th percentile range of the $\text{FWHM}_{\text{pred}}$ distribution as horizontal coloured bars for both samples. These values should only be taken as indicative as they depend heavily on the uncertain stellar masses and on the validity of the stellar mass to halo mass conversion.

Nevertheless, Fig. 7 reveals a very different pattern for our two redshift ranges. Many of our $z \sim 3.2$ LAEs have line widths substantially higher than what one would expect from their stellar masses, consistent with additional line broadening by Ly α radiative transfer effects. On the other hand, the observed line widths at $z \geq 6$ are in good agreement with the predicted line widths based on the stellar masses, with little evidence for significant further broadening. Below, we discuss the implications of this finding in connection with the observed differences in LAH properties.

6. Discussion

In the previous sections we presented evidence that the Ly α halo and also the spectral properties of our two samples of LAEs are very different between $z \geq 6$ and $z \sim 3$. We now discuss the implications of this finding in comparison with the literature and consider possible explanations.

6.1. How different are Ly α halo scale lengths at different redshifts?

We start with a brief review of the available evidence for and against major changes in the observed properties of Ly α haloes within the redshift range $3 \lesssim z \lesssim 6$. We focus here on LAHs around normal star-forming galaxies, leaving out the much brighter, much larger, and often AGN-related Ly α “nebulae” and “blobs”. Figure 8 shows a compilation of measured Ly α halo scale lengths from the literature plotted against redshift, including our new data. This diagram illustrates the conflicting trends seen in previous LAH observations: The stacking study by Momose et al. (2014) based on several thousands of LAEs in Subaru NB images found that the typical scale lengths stay essentially unchanged between $z = 2.2, 3.1,$ and 5.7 , with values around $\sim 5\text{--}10$ kpc, and rise to $r_{s,H} \simeq 12.6$ kpc at $z = 6.6$. In contrast, Wu et al. (2020), using similar data but a $3\times$ larger sample, measured a much smaller mean scale length of only ~ 2 kpc at $z = 5.7$. Kakuma et al. (2021) did not determine scale lengths, but reported no systematic differences in the stacked Ly α radial profiles of LAEs between $z = 5.7$ and 6.6 in their Subaru-HSC images.

The advent of individual LAH measurements with MUSE did initially not bring much more clarity. The first such study by LW16 of 21 LAHs in the Hubble Deep Field South suggested a tentative evolutionary trend that Ly α haloes might evolve towards gradually smaller sizes with increasing redshifts up to $z \lesssim 5.7$, but this trend was not deemed significant given the small sample. And indeed the nearly $10\times$ larger follow-up study by FL17 based on the MUSE-MOSAIC sample (Bacon et al. 2017) did not confirm such a trend, but concluded that LAH scale lengths do *not* change systematically within $3 \lesssim z \lesssim 6$. Guo et al. (2024b) found the same behaviour with stacking MUSE LAEs in bins of redshift from 3 to 6. That study also presented the first $z \geq 6$ LAH measurement with $r_{s,H} \simeq 3$ kpc. More recently, targeted MUSE observations of the outstandingly bright $z = 6.6$ Ly α emitter CR7 (Matthee et al. 2020a) and of the UV-luminous Lyman Break Galaxy VR7 at $z = 6.5$ (Matthee et al. 2020b) gave similar $r_{s,H}$ values of around 3 kpc.

A problem with all previous investigations is that results at different redshifts were obtained with roughly similar *apparent* SB sensitivities. After accounting for cosmological dimming this implies vastly different intrinsic SB detection limits between different redshift domains, which could have led to z -dependent biases in the estimation of LAH properties. Other possible obstacles to a proper comparison of results between studies are differences in the angular resolution of the data, as well as incompatible analysis methods.

Here we aimed at accounting for all these effects in a consistent way. In particular, as explained in Sect. 2.1 our data at $z \sim 3$ and $z \geq 6$ are fully matched in intrinsic surface brightness sensitivity (at the expense of giving up on sensitivity for the lower redshift range). The GLAO-improved PSF of the MUSE instrument provided the currently sharpest available view of LAEs, critical for our ability to constrain LAH scale lengths.

Figure 8 reveals that our results are strongly inconsistent with the null hypothesis of no evolution of LAH scale lengths from $z \geq 6$ to $z \sim 3$. Instead, we find that $z \geq 6$ LAHs are much smaller, by nearly a factor 3 in the mean, than their lower redshift siblings. In the right panel of Fig. 4 we compare the distributions of scale lengths of the detected haloes between our two samples. The marginal histograms indicate that they are very different in shape and peak location. A Kolmogorov-Smirnov test rules out

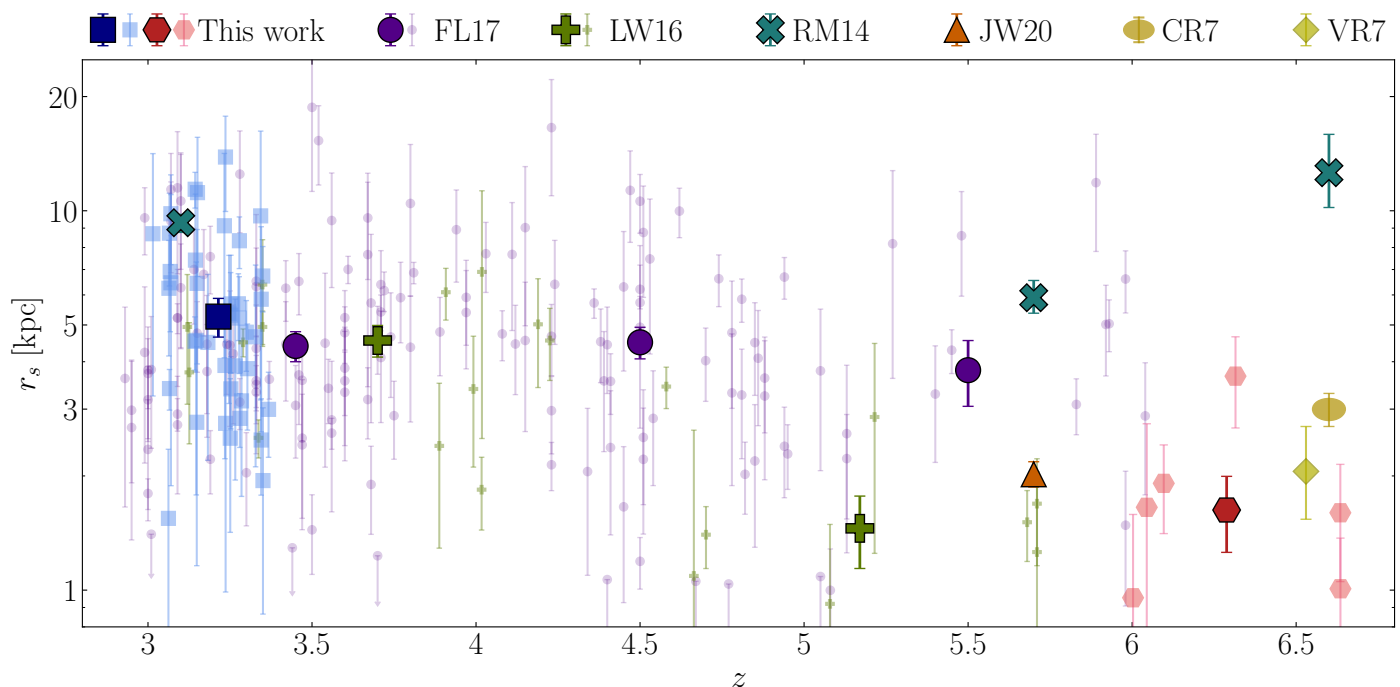


Fig. 8. Measured $\text{Ly}\alpha$ scale lengths as a function of redshift. The individually detected haloes from this study are shown as small squares ($z \sim 3.2$) and hexagons ($z \geq 6$), while sample median values are given by the big dark markers. These are compared to results from previous MUSE observations (LW16, FL17) and from stacking (Momose et al. 2014 – RM14, Wu et al. 2020 – JW20) as resolved in the legend, again with small symbols for individual measurements and big ones of the same marker type as median values. The MUSE measurements of CR7 (Matthee et al. 2020a) and VR7 (Matthee et al. 2020b) are also included.

the null hypothesis with high significance ($p = 0.0008$) that both samples are drawn from the same underlying population.

A possible caveat in this context could be differences in the physical characteristics – in particular the stellar masses (M_\star) of the galaxies between the two samples, since these are known to correlate (weakly) with LAH properties (Byrohl et al. 2021, Rasekh et al. 2022). We find that the $z \geq 6$ sample covers slightly lower stellar masses, but only by a factor ~ 2 – 3 , with mean values and rms scatter of $\log_{10}(M_\star/M_\odot)$ of the lower and higher redshift samples of 8.39 ± 0.77 and 7.75 ± 0.59 , respectively. The difference is mainly due to a larger fraction of relatively high mass galaxies ($M_\star \gtrsim 10^9 M_\odot$ in the $z \sim 3.2$ sample, while the lower mass bound is nearly the same for both datasets). The Bhattacharyya Distance (Bhattacharyya 1943) between the mass distributions of the two samples is 0.098, indicating a high degree of similarity.

We also checked that the $\text{Ly}\alpha$ luminosities and star formation rates (SFR) of the two samples are broadly similar. Note that while both samples are selected by their $\text{Ly}\alpha$ emission lines and thus approximately by SFR, the underlying surveys have very different depths so this similarity is not trivially fulfilled. The mean values and rms scatter of $\log_{10}[L_{\text{Ly}\alpha}/(\text{erg s}^{-1})]$ are 42.19 ± 0.32 and 41.58 ± 0.35 , respectively; for the star formation rates $\log_{10}[\text{SFR}/(M_\odot \text{ yr}^{-1})]$ resulting from our SED fitting we obtained 0.07 ± 0.75 and -0.35 ± 0.49 . The Bhattacharyya Distances between the $L_{\text{Ly}\alpha}$ and SFR distributions are 0.085 and 0.094, again confirming a high degree of overlap. Such small shifts of a factor ~ 2 – 3 in the mean is certainly insufficient to explain the differences between $z \geq 6$ and $z \sim 3.2$, considering the known large scatter in the relations between LAH scale lengths and other properties (FL17, Rasekh et al. 2022).

Moreover, the $z \sim 3$ subsample matched to the $z \geq 6$ in M_\star and/or SFR gives the same mean scale length and halo flux

fraction values. This further proves that the slight difference in the galaxy properties between our samples is not responsible for the drastic change in the halo properties.

While Fig. 4 contains only the individually detected $\text{Ly}\alpha$ haloes in our sample, we demonstrated in Sect. 4.3 and Fig. 6 that the differences between $z \sim 3$ and $z \geq 6$ LAHs become even more pronounced when comparing also the galaxies with undetected LAHs. We therefore conclude that the observed differences in $\text{Ly}\alpha$ halo sizes between $z \sim 3.2$ and $z \geq 6$ are not an artefact of drawing our LAE samples from very different parts of the galaxy population, but physically real and highly significant.

6.2. Are $\text{Ly}\alpha$ haloes at $z \geq 6$ smaller because of reionisation?

Since our high-redshift sample reaches into the late stages of the cosmic reionisation epoch (Planck Collaboration et al. 2016, Mangena et al. 2020, Umeda et al. 2026) which is known to affect the visibility of $\text{Ly}\alpha$ (Dijkstra 2014), it is conceivable that the changing conditions in the intergalactic and circumgalactic media associated with this fundamental phase transition also lead to different emerging $\text{Ly}\alpha$ haloes.

But how does a more neutral IGM and correspondingly higher $\text{Ly}\alpha$ optical depth change the observed properties of LAHs? For $\text{Ly}\alpha$ sources surrounded by a more or less homogeneous ambient medium following the Hubble flow the main effect will be to scatter the centrally emitted $\text{Ly}\alpha$ photons until they are redshifted out of resonance (Dijkstra 2014). For the modest optical depths of the post-reionisation period one would therefore expect that LAH scale lengths and $\text{Ly}\alpha$ line widths should get systematically larger with increasing neutral fraction and thus with redshift. When the reionisation epoch is reached this mechanism should result in very extended $\text{Ly}\alpha$ haloes stretching over intergalactic scales, with a strongly broadened line profile

(Loeb & Rybicki 1999, Park et al. 2021). Such haloes are probably unobservable individually due to their extremely low surface brightnesses (but might be detectable in large-scale line intensity mapping experiments; Padmanabhan & Loeb 2024), so that the scattered Ly α photons would be essentially lost from the observational budget.

This simple picture changes however when taking into account that Ly α emission from galaxies in an incompletely reionized Universe is detected mainly from sources in ionized bubbles (e.g., Trapp et al. 2023, Fujimoto et al. 2024, Neyer et al. 2025). The appearance of extended Ly α haloes will depend greatly on the properties of their host bubbles, in particular their sizes, which are still poorly constrained by observations. Numerical simulations have so far only provided a few indications of what to expect. In an early study, Smith et al. 2019 found that accounting for the evolving IGM transmission at $5 < z < 7$ actually steepens the emerging Ly α SB profiles and reduces their scale lengths by about 20% compared to the no IGM model. From their radiative transfer simulations, Park et al. (2021) concluded that large bubbles with radii of several comoving Mpc facilitate easier escape of Ly α photons than much smaller ones where some of the radiation would still diffuse to IGM scales and get effectively lost. However, their simulations lacked the resolution required to properly model the circumgalactic Ly α emission and make actual predictions for Ly α halo properties.

In the light of these theoretical arguments it seems that our observational results could indeed be interpreted, at least qualitatively, as driven by reionisation. In this scenario, most galaxies would reside in ionized bubbles large enough to allow the central emission to at least partly escape, but too small (or not sufficiently ionized) to avoid the diffusion of a large fraction of Ly α photons into the surrounding neutral regions, effectively suppressing the formation of detectable Ly α haloes. The few cases where we actually observe a resolved halo could then correspond to a somewhat larger host bubble.

Furthermore, recent deep observations of Ly α haloes studying radial evolution of the spectra discovered that the peak of the red wing of the Ly α line progressively moves towards the systemic velocity at larger radii (Gallego et al. 2021, Guo et al. 2024a, Mukherjee et al. 2026, Kozlova in prep.). Guo et al. (2024a) found tentative evidence that beyond 20 kpc the red peak even shifts blueward of the systemic velocity. If this behaviour is real and ubiquitous at high-redshift, it would also affect the Ly α halo sizes in the epoch of reionization. As the IGM transmission sharply drops to zero blueward of the systemic velocity, most of the blueshifted Ly α photons would get absorbed and/or scattered away thus decreasing the observed SB at larger radii. This would naturally produce more compact haloes at redshifts where IGM is still significantly neutral. However, due to the lack of robustly measured systemic redshifts and statistical nature of the study such a scenario remains mostly speculative.

This scenario seems particularly plausible if for $z < 6$ the properties of LAHs do *not* evolve much with redshift, at least down to $z \sim 3$, as suggested by the majority of previous studies (Momose et al. 2014, FL17, Kakuma et al. 2021 see Sect. 6.1). Note that this would imply a substantial amount of *intrinsic* evolution to counteract the strong population evolution of galaxies. Byrohl et al. (2021) investigated this question in a cosmological context using the TNG50 simulation and found that self-regulated feedback balancing inflows and outflows produces nearly redshift-invariant LAH sizes. In such a framework, a sudden change in halo sizes for galaxies at $z \geq 6$ would indeed have to be attributed mainly to the effects of reionisation.

Could the observed narrow Ly α line widths of the LAEs in our $z \geq 6$ sample also be an effect of the late stages of reionisation? A qualitatively similar phenomenon was already noted by Songaila et al. (2022) and Songaila et al. (2024) in a large spectroscopic follow-up study of bright LAEs selected from narrow-band imaging. They showed that at fixed Ly α luminosity, the Ly α line widths are on average smaller at $z = 6.6$ than at $z = 5.7$, and that this difference is stronger for objects of lower Ly α luminosities. Since our LAE sample is much fainter than theirs, by a full order of magnitude, we cannot compare directly, but extrapolating the trend from Songaila et al. (2024) between $L_{\text{Ly}\alpha}$ and $\text{FWHM}_{\text{Ly}\alpha}$ to the luminosity range of our $z \geq 6$ objects would yield a good agreement with our measured line widths.

To explain this fast change in FWHM from $z = 6.6$ to 5.7 , Songaila et al. (2024) suggested that the Ly α line widths experienced different amounts of truncation of their blue wings due to the rapidly evolving intervening Ly α Gunn-Peterson trough and damping wing. If this is correct then the same should apply to our sample. We find, however, much smaller line widths for our high-redshift objects, a decrease by a factor ~ 2.5 compared to $z \sim 3.2$ (see Fig. 7). To achieve such a strong reduction in the emergent line width would require quite extreme conditions, with negligible Ly α line offsets from systemic redshift as well as very small ionized bubble size, which seems somewhat unlikely (Verhamme et al. 2018, Prieto-Lyon et al. 2023, Saxena et al. 2024, Lu et al. 2024).

6.3. Or do Ly α halo sizes change in lockstep with galaxy evolution?

As an alternative scenario, we now consider the hypothesis that our finding of very different LAH sizes at $z \sim 3$ and $z \geq 6$ is just a reflection of the overall evolution of galaxy properties between these redshifts and not specifically connected to reionisation. In that case the effects of LAH evolution should be observable not just at $z \geq 6$ but at all redshifts, contradicting some – but not all – of the above mentioned studies. However, as already discussed in Sect. 6.1, the many pitfalls and potential biases arising from data quality and analysis aspects could so far have obscured the true evolutionary behaviour.

As a starting point for such a halo co-evolution scenario, we consider one of the most robust measured scaling relations hitherto found for LAHs, namely the correlation between Ly α and UV continuum scale lengths, $r_{s,H}^{\text{Ly}\alpha} \approx 10 \times r_{s,c}^{\text{UV}}$ (Steidel et al. 2011, LW16, FL17, Claeysens et al. 2022). If this relation is equally valid at all redshifts of interest, with a non-evolving proportionality factor, then together with the well-constrained general size evolution of galaxies (e.g., Shibuya et al. 2015, Paulino-Afonso et al. 2017, Ormerod et al. 2024, Ren et al. 2025, Yang et al. 2025), this necessarily implies a corresponding gradual growth of Ly α halo scale lengths with decreasing redshift. In quantitative terms, these studies find that galaxies grow in size by a factor 1.7–2.3 over the redshift range of interest – slightly smaller than the Ly α halo size ratio that we find, but close enough to explain the bulk of the halo size growth.

In this way our observed decrease of LAH sizes for $z \geq 6$ could thus simply be a consequence of the above correlation between halo and galaxy size holding also in the epoch of reionisation. Such a behaviour has already been observed for giant Ly α nebulae around quasars, which show a gradual size growth (e.g., Ginolfi et al. 2018, Momose et al. 2019, Farina et al. 2019, Bielby et al. 2020).

However, the growth of the galaxies’ stellar bodies is directly driven by and strongly coupled to the assembly of their dark matter haloes (Behroozi et al. 2019). In the same manner the CGM properties (its extent most importantly) are tightly linked to the dark matter halo and its virial parameters (e.g., Werk et al. 2014, Bordoloi et al. 2018, Lochhaas et al. 2020, Cook et al. 2025). Therefore, the growth of the dark matter haloes from $z \geq 6$ to $z \sim 3$ would naturally explain the increase in the Ly α halo sizes.

To test this hypothesis, we estimated the virial radii of galaxies in both samples based on the halo masses derived in Sect. 5. We find that at $z \sim 3$ the typical virial radius in our sample is 2.6 times larger than at $z \geq 6$ (35 kpc and 13 kpc, respectively), a difference remarkably similar to the difference between the Ly α scale lengths. We find the ratio between LAH scale length and virial radius to be 0.16 across both samples. If our estimates of the halo masses (and hence virial radii) are correct, this similarity would naturally imply that the growth of the Ly α haloes is naturally directly tied to the assembly of the dark matter halo reinforcing the gradual evolutionary scenario.

Since the spatial extent over which Ly α gets scattered by circumgalactic gas depends strongly on the H I fraction, we can try to link the expected evolution of Ly α haloes to the general H I content of the Universe. The latter is traced directly by the incidence rate of damped Ly α absorbers (DLAs) that can be observed in quasar spectra up to $z \sim 5$ (but not beyond due to the ever increasing obscuration by the Ly α forest). Earlier measurements suggested that the cosmic H I density increases steadily towards higher redshifts (Bird et al. 2017, Ho et al. 2021, Rhee et al. 2023; see also the review by Péroux & Howk 2020). In the absence of other effects, this would imply that Ly α haloes would be larger at earlier cosmic times (see Sect. 6.2), contrary to the size evolution trend of galaxies. Recently, however, Oyarzún et al. (2025) reported a maximum in the DLA incidence rate at $z \sim 4 - 4.5$ and a decline beyond. The authors interpret this as evidence in support of a gradual build-up of the baryonic content of galaxies over cosmic time. If confirmed, then this should result in a likewise gradual growth of the Ly α scattering medium, in lockstep with their central galaxies.

7. Conclusions

In this paper we took advantage of the unprecedented sensitivity of the MUSE Extremely Deep Field to perform the first systematic investigation of the properties of Ly α haloes around Ly α emitters at redshifts $z \geq 6$. We find remarkably strong ensemble differences to a comparison sample at lower redshifts around $z \sim 3.2$, carefully selected to be observed at similar intrinsic surface brightness sensitivity after accounting for cosmological SB dimming. Our results can be summarized as follows:

- (i) We identify significantly extended Ly α emission around 6 individual high-redshift LAEs from our sample of 18 objects. This more than doubles the number of known Ly α haloes beyond $z = 6$ and provides the first statistical set of LAHs associated with low-luminosity, low-mass systems at these redshifts (Fig. 5).
- (ii) The sizes (scale lengths) of these 6 high- z Ly α haloes are much smaller than those of typical lower redshift LAEs with similar Ly α luminosities and stellar masses, by about a factor 3 in the mean. Their Ly α halo flux fractions are however similarly high as at lower z with values around 0.6 (Fig. 4).
- (iii) Stacking the remaining 12 LAEs with individually undetected Ly α haloes does not lead to the detection of a mean

LAH signal, not even a tentative trace (Fig. 6). Thus, nearly 70% of LAEs at these high redshifts have either no Ly α halo at all, or only a very weak or small one.

- (iv) In stark contrast, combining our $z \sim 3.2$ objects without individual LAH detections recovers a highly significant Ly α halo in the stacked data (Fig. 6), indicating broadly similar LAH properties for the entire sample. Overall, our results for the lower redshift comparison sample are in excellent agreement with those of previous studies.
- (v) Comparing our $z \geq 6$ measurements with the results of previous observations for this redshift range is not straightforward as the few available studies show a large dispersion. Our data rule out any previous suggestions that LAHs do not evolve at $z \geq 6$ or are systematically larger (Fig. 8).
- (vi) We also measure substantially lower Ly α line widths of the $z \geq 6$ LAEs, by a factor ~ 2.5 compared to similar lower redshift objects (Fig. 7). The lines of the high- z LAEs are often so narrow (but still resolved by MUSE) that the inferred amount of broadening by radiative transfer effects must be quite modest relative to the predicted intrinsic virial line widths based on stellar masses from SED fitting.

Our results provide important constraints on the propagation of Ly α photons during the late stages of reionisation, and on the evolution of the CGM in general. However, the question about the physical origin for the observed differences in LAH properties must for the moment stay open. We considered two possible broad scenarios, one in which the transition from a partly neutral to a highly ionized IGM results in a rapid change of Ly α scattering and visibility behaviour, and an alternative scenario of “slow” co-evolution between the general population of star forming galaxies and their Ly α haloes.

In the reionisation-dominated scenario (see Sect. 6.2) it would be tempting to build a direct connection between the small sizes and frequent undetectability of Ly α haloes and the measured narrow Ly α line profiles, both of which are believed to be strongly shaped by resonant scattering. It could be that the Ly α radiation that we receive from low-luminosity LAEs is composed mainly of those Ly α photons that escaped with a relatively modest scattering history, both spatially (escaping closer to the sites of star formation) and spectrally (escaping closer to systemic redshift). The remainder of the total escaping Ly α radiation would then be suffering much stronger scattering than at lower redshifts, producing a vast but probably unobservable halo due to its low surface brightness and strongly broadened line profile.

Such effects would also provide a natural explanation for the apparent non-evolution of the Ly α luminosity function at $3 \leq z \leq 6$ and its rapid decrease beyond $z \approx 6$ (Umeda et al. 2025). A substantial loss of Ly α photons to the still partly neutral IGM would result in systematically lower recovered Ly α luminosities at $z \geq 6$. Another relevant finding of this study is that the two main drivers of LAE detectability – halo size and spectral line width (Pharo et al. 2024) – show drastic redshift evolution, affecting the LAE selection function and hence strongly influencing the Ly α luminosity function. Thus, the prominence and sizes of Ly α haloes has the potential to serve as an additional powerful diagnostic for the properties of the ionized regions where LAEs are found, especially in conjunction with high-resolution radiative transfer simulations.

On the other hand, it is also possible that the previously held view, supported by a number of studies (e.g., Momose et al. 2014, FL17), of more or less unevolving Ly α halo properties between $z \sim 3$ and $z \sim 6$ is incorrect, and that Ly α halo sizes grow

more or less in lockstep with their host galaxies (Sect. 6.3). This is fortunately a testable hypothesis, as data of sufficient quality exist. A systematic investigation of Ly α halo properties over the full redshift range accessible to MUSE, using improved analysis methods and taking advantage of the latest generation of GLAO-supported MUSE deep fields including the MXDF and the MUSCATEL survey, should firmly establish how the relation between galaxies and their surrounding LAHs evolve. We have started with such an analysis and aim to report on the outcome in a future paper.

Such a galaxy-LAH coevolution framework would certainly have the appeal of not requiring any special modelling treatment for LAHs at the highest redshifts. The question is whether this is physically plausible under the changing conditions during the late stages and aftermath of reionisation. Another possible problem with this scenario is that in general one should expect the *minimum* Ly α line widths to scale with the cosmologically growing host masses. The fact that our two LAE samples display very different FWHM_{Ly α} values, at similar stellar mass distributions, is therefore not in obvious agreement with the simplest coevolution scenario. However, we emphasize that the two scenarios sketched above are by no means mutually exclusive. It is possible that both are required for a full explanation of our observations, a global evolutionary trend *and* changes in Ly α escape properties that are specific to the late stages of reionisation.

Acknowledgements. This project has received funding from the European Research Council (ERC) under the European Union's Horizon 2020 research and innovation programme (grant agreement 101020943, SPECMAP-CGM). This work made use of the following software packages: `astropy` (Astropy Collaboration et al. 2013, 2018, 2022), `matplotlib` (Hunter 2007), `numpy` (Harris et al. 2020), `pandas` (Wes McKinney 2010; pandas development team 2026), `python` (Van Rossum & Drake 2009), `scipy` (Virtanen et al. 2020; Gommers et al. 2026), `scikit-image` (van der Walt et al. 2014), and `TOPCAT` (Taylor 2005). This research made use of `Photutils`, an Astropy package for detection and photometry of astronomical sources (Bradley et al. 2025). Software citation information aggregated using The Software Citation Station (Wagg & Broekgaarden 2024; Wagg et al. 2025).

References

- Ahn, K. & Shapiro, P. R. 2021, *ApJ*, 914, 44
- Arrigoni Battaia, F., Hennawi, J. F., Prochaska, J. X., et al. 2019, *MNRAS*, 482, 3162
- Astropy Collaboration, Price-Whelan, A. M., Lim, P. L., et al. 2022, *ApJ*, 935, 167
- Astropy Collaboration, Price-Whelan, A. M., Sipőcz, B. M., et al. 2018, *AJ*, 156, 123
- Astropy Collaboration, Robitaille, T. P., Tollerud, E. J., et al. 2013, *A&A*, 558, A33
- Bacon, R., Accardo, M., Adjali, L., et al. 2010, in *Society of Photo-Optical Instrumentation Engineers (SPIE) Conference Series*, Vol. 7735, *Ground-based and Airborne Instrumentation for Astronomy III*, ed. I. S. McLean, S. K. Ramsay, & H. Takami, 773508
- Bacon, R., Brinchmann, J., Conseil, S., et al. 2023, *A&A*, 670, A4
- Bacon, R., Brinchmann, J., Richard, J., et al. 2015, *A&A*, 575, A75
- Bacon, R., Conseil, S., Mary, D., et al. 2017, *A&A*, 608, A1
- Behroozi, P., Wechsler, R. H., Hearin, A. P., & Conroy, C. 2019, *MNRAS*, 488, 3143
- Behroozi, P. S., Wechsler, R. H., & Conroy, C. 2013, *ApJ*, 770, 57
- Bhattacharyya, A. 1943, *Bulletin of the Calcutta Mathematical Society*, 35, 99
- Bielby, R. M., Fumagalli, M., Fossati, M., et al. 2020, *MNRAS*, 493, 5336
- Bird, S., Garnett, R., & Ho, S. 2017, *MNRAS*, 466, 2111
- Blaizot, J., Garel, T., Verhamme, A., et al. 2023, *MNRAS*, 523, 3749
- Bordoloi, R., Prochaska, J. X., Tumlinson, J., et al. 2018, *ApJ*, 864, 132
- Borisova, E., Cantalupo, S., Lilly, S. J., et al. 2016, *ApJ*, 831, 39
- Bradley, L., Sipőcz, B., Robitaille, T., et al. 2025, *astropy/photutils*: 2.3.0
- Bruzual, G. & Charlot, S. 2003, *MNRAS*, 344, 1000
- Bunker, A. J., Cameron, A. J., Curtis-Lake, E., et al. 2024, *A&A*, 690, A288
- Byler, N., Dalcanton, J. J., Conroy, C., & Johnson, B. D. 2017, *ApJ*, 840, 44
- Byrohl, C., Nelson, D., Behrens, C., et al. 2021, *MNRAS*, 506, 5129
- Calzetti, D., Armus, L., Bohlin, R. C., et al. 2000, *ApJ*, 533, 682
- Chabrier, G. 2003, *PASP*, 115, 763
- Chen, Z., Stark, D. P., Mason, C., et al. 2024, *MNRAS*, 528, 7052
- Claeysens, A., Richard, J., Blaizot, J., et al. 2022, *A&A*, 666, A78
- Comparat, J., Zhu, G., Gonzalez-Perez, V., et al. 2016, *MNRAS*, 461, 1076
- Conroy, C. & Gunn, J. E. 2010, *ApJ*, 712, 833
- Conroy, C., Gunn, J. E., & White, M. 2009, *ApJ*, 699, 486
- Cook, A. W. S., van de Voort, F., Pakmor, R., & Grand, R. J. J. 2025, *MNRAS*, 543, 1224
- Cullen, F., McLure, R. J., Dunlop, J. S., et al. 2020, *MNRAS*, 495, 1501
- Curtis-Lake, E., Cameron, A. J., Bunker, A. J., et al. 2026, *MNRAS*[arXiv:2510.01033]
- D'Eugenio, F., Cameron, A. J., Scholtz, J., et al. 2025, *ApJS*, 277, 4
- Dijkstra, M. 2014, *PASA*, 31, e040
- Eisenstein, D. J., Willott, C., Alberts, S., et al. 2023, *arXiv e-prints*, arXiv:2306.02465
- Evrard, A. E., Bialek, J., Busha, M., et al. 2008, *ApJ*, 672, 122
- Farina, E. P., Arrigoni-Battaia, F., Costa, T., et al. 2019, *ApJ*, 887, 196
- Farina, E. P., Venemans, B. P., Decarli, R., et al. 2017, *ApJ*, 848, 78
- Fujimoto, S., Wang, B., Weaver, J. R., et al. 2024, *ApJ*, 977, 250
- Gallego, S. G., Cantalupo, S., Sarpas, S., et al. 2021, *MNRAS*, 504, 16
- Ginolfi, M., Maiolino, R., Carniani, S., et al. 2018, *MNRAS*, 476, 2421
- Gommers, R., Virtanen, P., Haberland, M., et al. 2026, *scipy/scipy*: SciPy 1.17.1
- Gronke, M. 2017, *A&A*, 608, A139
- Guo, Y., Bacon, R., Wisotzki, L., et al. 2024a, *A&A*, 691, A66
- Guo, Y., Bacon, R., Wisotzki, L., et al. 2024b, *A&A*, 688, A37
- Harris, C. R., Millman, K. J., van der Walt, S. J., et al. 2020, *Nature*, 585, 357
- Hayes, M. J., Runnholm, A., Gronke, M., & Scarlata, C. 2021, *ApJ*, 908, 36
- Herenz, E. C. 2023, *Astronomische Nachrichten*, 344, e20220091
- Herenz, E. C. & Wisotzki, L. 2017, *A&A*, 602, A111
- Ho, M.-F., Bird, S., & Garnett, R. 2021, *MNRAS*, 507, 704
- Hunter, J. D. 2007, *Computing in Science & Engineering*, 9, 90
- Kageura, Y., Ouchi, M., Nakane, M., et al. 2025, *ApJS*, 278, 33
- Kakuma, R., Ouchi, M., Harikane, Y., et al. 2021, *ApJ*, 916, 22
- Kikuchi, S., Harikane, Y., Ouchi, M., et al. 2022, *ApJ*, 931, 97
- Kiyota, T., Ouchi, M., Xu, Y., et al. 2025, *ApJ*, 995, 150
- Kriek, M., van Dokkum, P. G., Labbé, I., et al. 2009, *ApJ*, 700, 221
- Kusakabe, H., Shimasaku, K., Momose, R., et al. 2019, *PASJ*, 71, 55
- Leclercq, F., Bacon, R., Verhamme, A., et al. 2020, *A&A*, 635, A82
- Leclercq, F., Bacon, R., Wisotzki, L., et al. 2017, *A&A*, 608, A8
- Lochhaas, C., Bryan, G. L., Li, Y., Li, M., & Fielding, D. 2020, *MNRAS*, 493, 1461
- Loeb, A. & Rybicki, G. B. 1999, *ApJ*, 524, 527
- Lotz, J. M., Koekemoer, A., Coe, D., et al. 2017, *ApJ*, 837, 97
- Lower, S., Narayanan, D., Leja, J., et al. 2020, *ApJ*, 904, 33
- Lu, T.-Y., Mason, C. A., Hutter, A., et al. 2024, *MNRAS*, 528, 4872
- Mangena, T., Hassan, S., & Santos, M. G. 2020, *MNRAS*, 494, 600
- Marconcini, C., D'Eugenio, F., Maiolino, R., et al. 2025, *A&A*, 699, A154
- Mason, C. A. & Gronke, M. 2020, *MNRAS*, 499, 1395
- Matthee, J., Pezzulli, G., Mackenzie, R., et al. 2020a, *MNRAS*, 498, 3043
- Matthee, J., Sobral, D., Gronke, M., et al. 2020b, *MNRAS*, 492, 1778
- McKay, B., Tuttle, S., Cooper, E. M., et al. 2026, *ApJ*, 1001, 150
- Melia, F. 2024, *A&A*, 689, A10
- Mitchell, P. D., Blaizot, J., Cadiou, C., et al. 2021, *MNRAS*, 501, 5757
- Momose, R., Goto, T., Utsumi, Y., et al. 2019, *MNRAS*, 488, 120
- Momose, R., Ouchi, M., Nakajima, K., et al. 2014, *MNRAS*, 442, 110
- Mukherjee, T., Zafar, T., Nanayakkara, T., et al. 2026, *PASA*, 43, e021
- Muzahid, S., Schaye, J., Marino, R. A., et al. 2020, *MNRAS*, 496, 1013
- Napolitano, L., Pentericci, L., Santini, P., et al. 2024, *A&A*, 688, A106
- Neyer, M., Smith, A., Vogelsberger, M., et al. 2025, *arXiv e-prints*, arXiv:2510.18946
- Ormerod, K., Conselice, C. J., Adams, N. J., et al. 2024, *MNRAS*, 527, 6110
- Ouchi, M., Ono, Y., Egami, E., et al. 2009, *ApJ*, 696, 1164
- Ouchi, M., Ono, Y., & Shibuya, T. 2020, *ARA&A*, 58, 617
- Oyarzún, G. A., Rafelski, M., Christensen, L., et al. 2025, *ApJ*, 983, 10
- Padmanabhan, H. & Loeb, A. 2024, *arXiv e-prints*, arXiv:2408.16820
- Pagul, A., Sánchez, F. J., Davidzon, I., & Mobasher, B. 2021, *ApJS*, 256, 27
- pandas development team, T. 2026, *pandas-dev/pandas*: Pandas
- Park, H., Jung, I., Song, H., et al. 2021, *ApJ*, 922, 263
- Partridge, R. B. & Peebles, P. J. E. 1967, *ApJ*, 147, 868
- Paulino-Afonso, A., Sobral, D., Buitrago, F., & Afonso, J. 2017, *MNRAS*, 465, 2717
- Pelliccia, D., Strait, V., Lemaux, B. C., et al. 2021, *ApJ*, 908, L30
- Peng, C. Y., Ho, L. C., Impey, C. D., & Rix, H.-W. 2002, *AJ*, 124, 266
- Peng, C. Y., Ho, L. C., Impey, C. D., & Rix, H.-W. 2010, *AJ*, 139, 2097
- Péroux, C. & Howk, J. C. 2020, *ARA&A*, 58, 363
- Pessa, I., Wisotzki, L., Urrutia, T., et al. 2026, *A&A*, 708, A214
- Pharo, J., Wisotzki, L., Urrutia, T., et al. 2024, *A&A*, 690, A343
- Planck Collaboration, Adam, R., Aghanim, N., et al. 2016, *A&A*, 596, A108
- Prieto-Lyon, G., Mason, C., Mascia, S., et al. 2023, *ApJ*, 956, 136
- Rasekh, A., Melinder, J., Östlin, G., et al. 2022, *A&A*, 662, A64

- Ren, J., Liu, F. S., Li, N., et al. 2025, *ApJ*, 982, 200
- Rhee, J., Meyer, M., Popping, A., et al. 2023, *MNRAS*, 518, 4646
- Runnholm, A., Hayes, M. J., Mehta, V., et al. 2025, *ApJ*, 984, 95
- Saxena, A., Bunker, A. J., Jones, G. C., et al. 2024, *A&A*, 684, A84
- Saxena, A., Robertson, B. E., Bunker, A. J., et al. 2023, *A&A*, 678, A68
- Schmidt, K. B., Kerutt, J., Wisotzki, L., et al. 2021, *A&A*, 654, A80
- Scholtz, J., Carniani, S., Parlanti, E., et al. 2026, *MNRAS*[arXiv:2510.01034]
- Shibuya, T., Ouchi, M., & Harikane, Y. 2015, *ApJS*, 219, 15
- Shibuya, T., Ouchi, M., Harikane, Y., et al. 2018, *PASJ*, 70, S15
- Shipley, H. V., Lange-Vagle, D., Marchesini, D., et al. 2018, *ApJS*, 235, 14
- Smith, A., Ma, X., Bromm, V., et al. 2019, *MNRAS*, 484, 39
- Songaila, A., Barger, A. J., Cowie, L. L., Hu, E. M., & Taylor, A. J. 2022, *ApJ*, 935, 52
- Songaila, A., Cowie, L. L., Barger, A. J., Hu, E. M., & Taylor, A. J. 2024, *ApJ*, 971, 136
- Steidel, C. C., Bogosavljević, M., Shapley, A. E., et al. 2011, *ApJ*, 736, 160
- Tang, M., Stark, D. P., Ellis, R. S., et al. 2024, *MNRAS*, 531, 2701
- Taylor, M. B. 2005, in *Astronomical Society of the Pacific Conference Series*, Vol. 347, *Astronomical Data Analysis Software and Systems XIV*, ed. P. Shopbell, M. Britton, & R. Ebert, 29
- Trapp, A. C., Furlanetto, S. R., & Davies, F. B. 2023, *MNRAS*, 524, 5891
- Umeda, H., Ouchi, M., Kageura, Y., et al. 2026, *ApJ*, 997, 86
- Umeda, H., Ouchi, M., Kikuta, S., et al. 2025, *ApJS*, 277, 37
- Urrutia, T., Wisotzki, L., Kerutt, J., et al. 2019, *A&A*, 624, A141
- van der Walt, S., Schönberger, J. L., Nunez-Iglesias, J., et al. 2014, *PeerJ*, 2, e453
- Van Rossum, G. & Drake, F. L. 2009, *Python 3 Reference Manual* (Scotts Valley, CA: CreateSpace)
- Verhamme, A., Garel, T., Ventou, E., et al. 2018, *MNRAS*, 478, L60
- Verhamme, A., Schaerer, D., & Maselli, A. 2006, *A&A*, 460, 397
- Virtanen, P., Gommers, R., Oliphant, T. E., et al. 2020, *Nature Methods*, 17, 261
- Wagg, T., Broekgaarden, F., Van-Lane, P., Wu, K., & Gültekin, K. 2025, *TomWagg/software-citation-station: v1.4*
- Wagg, T. & Broekgaarden, F. S. 2024, *arXiv e-prints*, arXiv:2406.04405
- Weilbacher, P. M., Palsa, R., Streicher, O., et al. 2020, *A&A*, 641, A28
- Werk, J. K., Prochaska, J. X., Tumlinson, J., et al. 2014, *ApJ*, 792, 8
- Wes McKinney. 2010, in *Proceedings of the 9th Python in Science Conference*, ed. Stéfan van der Walt & Jarrod Millman, 56 – 61
- Wisotzki, L., Bacon, R., Blaizot, J., et al. 2016, *A&A*, 587, A98
- Witstok, J., Jakobsen, P., Maiolino, R., et al. 2025, *Nature*, 639, 897
- Wu, J., Jiang, L., & Ning, Y. 2020, *ApJ*, 891, 105
- Yang, L., Kartaltepe, J. S., Franco, M., et al. 2025, *ApJS*, 281, 68
- Zhang, H., Ouchi, M., Itoh, R., et al. 2020, *ApJ*, 891, 177

Appendix A: Stacks

Figure A.1 shows the SB profiles of stacked NB images of all galaxies in each sample, as well as those with or without a detected halo.

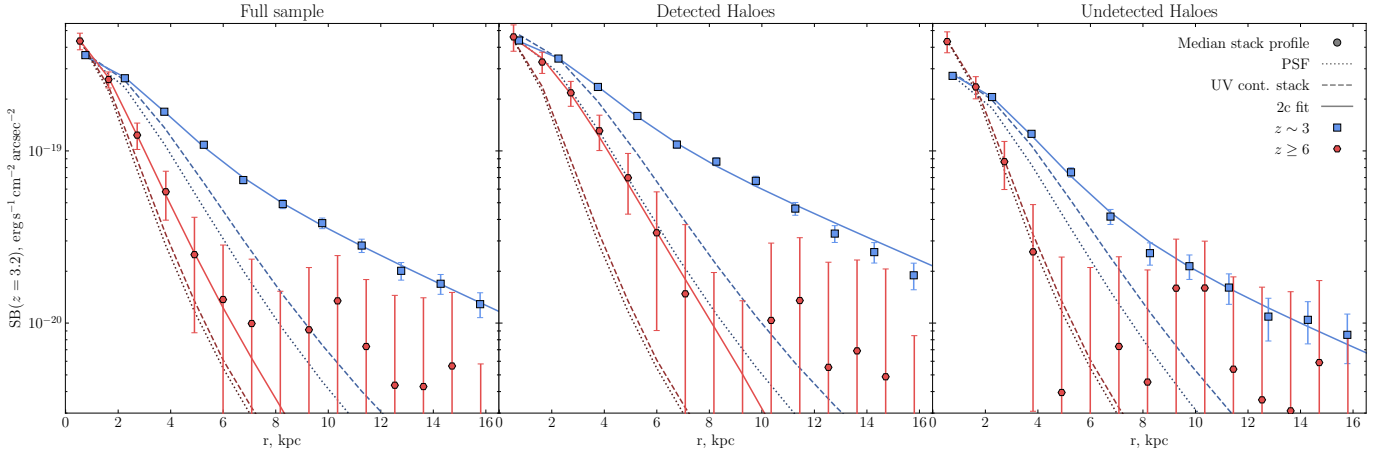


Fig. A.1. Median Ly α surface brightness profiles of various samples of LAEs. *Left panel* shows the median stacks of all LAEs in the $z \sim 3$ and $z \geq 6$ samples, while *central* and *right panels* depict sources with and without individually detected Ly α haloes. Measured data is shown in blue squares ($z \sim 3$ sample) and red hexagons ($z \geq 6$ sample). For an easier comparison, the high-redshift measurement is shifted to $z = 3.2$ – median redshift of the lower- z sample. PSF UV continuum stack SB profiles are shown in dotted and dashed lines respectively. The solid line shows a SB profile of a 2 component fit to the NB stacked data.

Appendix B: Upper limits of undetected Ly α haloes

5 To determine the limiting parameters of haloes around LAEs that were not detected in this study, we conduct the following experiment. For each such object we generate a grid of mock haloes varying scale length and the halo flux fraction while fixing the axis ratio to 1. Each mock halo was then added to the extracted
 10 NB image of the source and fed to the detection procedure described in Sect. 3.2. On the resulting grid of χ^2 values in the $r_{s,H}-f_H$ plane we determine the *detection* upper limit as a χ^2 contour corresponding to $p_0 = 0.05$. Fig. B.1 shows derived upper limits of undetected haloes in both samples with detected objects also superposed. The emergent upper limit curves have a typical
 15 U shape as it is hard to distinguish a very compact halo from the central component and detect a very extended and hence a low SB halo. The change in the upper limits between the two samples is very similar to the change in detected halo properties seen in Fig. 4: while the f_H constraints span the same parameter
 20 space, upper limit curves reach minima at smaller $r_{s,H}$ values at higher redshift. We also show parameters inferred from fitting a 2 component model to the stacked narrowband data. As one would expect, the undetected halo stack resides in the lower f_H region of the plot, compared to the detected population below most of the upper limits lines, while the detected halo stack is more similar to the individual objects. Based on behaviour of the $z \sim 3$
 25 stacks, it is possible to put the upper limits on the parameters of $z \geq 6$ undetected halo stack as $f_H \lesssim 0.4$ and $r_{s,H} \lesssim 1.3$ kpc.

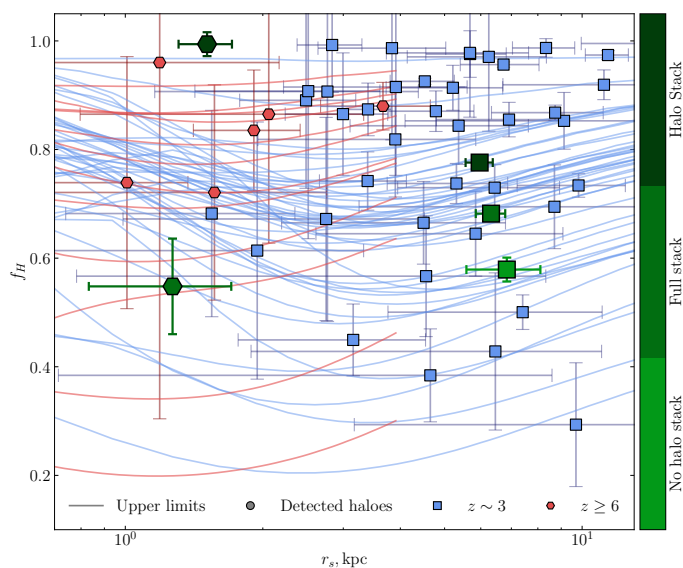


Fig. B.1. Upper limits of undetected objects compared to properties of individual LAEs and stacks. Curves show the upper limits for undetected haloes and markers show measurements of individual haloes, both colour coded by sample. Parameters measured from the stacked images are represented by large markers with the type of stack encoded by shade of green.

30 Appendix C: Resolution effects and the recovery of Ly α halo sizes

Another possible effects that might influence the observed scale length distributions are a change in PSF size and angular diameter distance (D_A) evolution. As D_A decreases with redshift
 35 beyond $z = 1.6$, objects of the same physical size become apparently more extended. In the context of this study, this constitutes a factor 1.4 increase in the apparent size of the objects

at $z \approx 6$ compared to $z \approx 3$, which increases the detectability of compact haloes. The change of the MUSE PSF size with wavelength also introduces a dependence of the LAH detection threshold on redshift. As the detection procedure compares the UV continuum model convolved with the MUSE PSF at the observed wavelength, this dependence is linear in PSF FWHM to first order. A typical ratio between PSF FWHM at 5105 Å ($z_{Ly\alpha} = 3.2 \approx \langle z_{MUSCATEL} \rangle$) and 8860 Å ($z_{Ly\alpha} = 6.29 \approx \langle z_{MXDF} \rangle$) is 1.5. Both these effects combined increase the minimal size of a detectable LAH by a factor of 2 when comparing high-redshift LAEs to lower- z ones. To test this, we conducted a simple experiment: using derived GALFIT models, we created mock NB images of the high- z LAEs at $z = 3.2$, taking into account both PSF broadening and angular size decrease. We then applied our detection algorithm to mock images under MUSCATEL-SF conditions and recovered only 3 haloes (out of 6), all of which have $r_{s,H} > 2$ kpc, which is very close to twice the minimal $r_{s,H}$ detected in the MXDF sample. Thus, this effect can explain the apparent lack of compact ($r_{s,H} \lesssim 2$ kpc) haloes in the $z \sim 3$ sample. The observed discrepancy could be solved statistically by assuming all LAEs in the MUSCATEL sample without a detected LAH to host a compact halo below the limit with $1 \text{ kpc} \lesssim r_{s,H} \lesssim 2 \text{ kpc}$. However, studies with higher SB sensitivity and hence lower $r_{s,H}$ detection limit do not find such an overabundance of compact haloes (LW16, FL17, Pharo et al. 2024), making this assumption unreasonable. Moreover, this argument does not explain the absence of large haloes in the high-redshift sample since such objects lie sufficiently above the detection limit.